SANDIA REPORT

SAND2006-5920
Unlimited Release
Printed October 2006

Modeling Brittle Fracture, Slip Weakening, and Variable Friction in Geomaterials with an Embedded Strong Discontinuity Finite Element

Craig D. Foster, Richard A. Regueiro and Ronaldo I. Borja

Prepared by
Sandia National Laboratories
Albuquerque, New Mexico 87185 and Livermore, California 94550

Sandia is a multiprogram laboratory operated by Sandia Corporation,
a Lockheed Martin Company, for the United States Department of Energy's
National Nuclear Security Administration under Contract DE-AC04-94-AL85000.

Sandia National Laboratories

Issued by Sandia National Laboratories, operated for the United States Department of Energy by Sandia Corporation.

Available to DOE and DOE contractors from
U.S. Department of Energy
Office of Scientific and Technical Information
P.O. Box 62
Oak Ridge, TN 37831

Telephone:	(865) 576-8401
Facsimile:	(865) 576-5728
E-Mail:	reports@adonis.osti.gov
Online ordering:	http://www.osti.gov/bridge

Available to the public from
U.S. Department of Commerce
National Technical Information Service
5285 Port Royal Rd
Springfield, VA 22161

Telephone:	(800) 553-6847
Facsimile:	(703) 605-6900
E-Mail:	orders@ntis.fedworld.gov
Online ordering:	http://www.ntis.gov/help/ordermethods.asp?loc=7-4-0#online

SAND2006-5920
Unlimited Release
Printed October 2006

Modeling Brittle Fracture, Slip Weakening, and Variable Friction in Geomaterials with an Embedded Strong Discontinuity Finite Element

Craig D. Foster and Ronaldo I. Borja
Department of Civil and Environmental Engineering
Stanford University
M.C. 4020
Stanford, CA 94305
cfoster01@yahoo.com
borja@stanford.edu

Richard A. Regueiro
Department of Civil, Environmental and Architectural Engineering
University of Colorado at Boulder
1111 Engineering Dr
428 UCB, ECOT 441
Boulder, CO 80309
Richard.Regueiro@Colorado.edu

Abstract

Localized shear deformation plays an important role in a number of geotechnical and geological processes. Slope failures, the formation and propagation of faults, cracking in concrete dams, and shear fractures in subsiding hydrocarbon reservoirs are examples of important effects of shear localization. Traditional engineering analyses of

these phenomena, such as limit equilibrium techniques, make certain assumptions on the shape of the failure surface as well as other simplifications. While these methods may be adequate for the applications for which they were designed, it is difficult to extrapolate the results to more general scenarios.

An alternative approach is to use a numerical modeling technique, such as the finite element method, to predict localization. While standard finite elements can model a wide variety of loading situations and geometries quite well, for numerical reasons they have difficulty capturing the softening and anisotropic damage that accompanies localization. By introducing an enhancement to the element in the form of a fracture surface at an arbitrary position and orientation in the element, we can regularize the solution, model the weakening response, and track the relative motion of the surfaces.

To properly model the slip along these surfaces, the traction-dispalcement response must be properly captured. This report focuses on the development of a constitutive model appropriate to localizing geomaterials, and the embedding of this model into the enhanced finite element framework. This modeling covers two distinct phases. The first, usually brief, phase is the weakening response as the material transitions from intact continuum to a body with a cohesionless fractured surface. Once the cohesion has been eliminated, the response along the surface is completely frictional. We have focused on a rate- and state-dependent frictional model that captures stable and unstable slip along the surface. This model is embedded numerically into to the element using a generalized trapezoidal formulation. While the focus is on the constitutive model of interest, the framework is also developed for a general surface response.

This report summarizes the major research and development accomplishments for the LDRD project titled "Cohesive Zone Modeling of Failure in Geomaterials: Formulation and Implementation of a Strong Discontinuity Model Incorporating the Effect of Slip Speed on Frictional Resistance". This project supported a strategic partnership between Sandia National Laboratories and Stanford University by providing funding for the lead author, Craig Foster, during his doctoral research.

Keywords: shear fracture; geomaterials; bifurcation; enhanced strain; finite element; rate- and state-friction

Contents

List of Figures

List of Tables

This page intentionally left blank.

Chapter 1

Introduction

This report summarizes the major research and development accomplishments for the LDRD project titled "Cohesive Zone Modeling of Failure in Geomaterials: Formulation and Implementation of a Strong Discontinuity Model Incorporating the Effect of Slip Speed on Frictional Resistance". This project supported a strategic partnership between Sandia National Laboratories and Stanford University by providing funding for the lead author, Craig Foster, during his doctoral research.

1.1 Background and motivation

The phenomenon of localized deformation has received a great deal of attention in the engineering and science communities over the past few decades. Localized deformation refers to intense straining over narrow regions in a body, while the majority of the body is undergoing far less deformation. This type of deformation has been observed in a variety of materials. Examples include shear banding and necking in metals, necking in polymers, and shear fracturing in bulk metallic glasses. In geomaterials we observe shear, compaction, and dilatation bands in porous rocks; shear and tensile fractures in more brittle rocks, ceramics, and concrete; shear bands in sands, and cracking in heavily overconsolidated clays.

The importance of localization is two-fold. First, the intense straining can lead to large displacements that significantly change shape of the structure, altering how it performs. Perhaps more importantly, the intense straining affects the properties of the material, and hence the structure. Compaction bands decrease the porosity of the material, and hence the permeability across the band. This change has implications to the recovery of fluids from hydrocarbon reservoirs, and also changes the drainage of the site. Dilatation bands have the opposite effect on permeability. While in both of these examples the mechanical properties of these material may also change, the change in mechanical response is typically more dramatic for materials undergoing shear localization. In this case, any cohesive strength of the parent material is typically degraded, often rapidly depending on the material's ductility. The weakening along these bands can be responsible for structural failure. Slope failures, fractures in concrete dams, rock fall and rock burst in tunnel excavations, and folding and faulting

of geological formations are examples of some of the results of localized deformation in geomaterials.

1.2 Mechanics of localization

The prediction of localized deformation and its effects is still a non-trivial task, especially in geomaterials where considerable uncertainty may exist in the characterization of the material. Roughly, we can divide the problem into four areas. First, to understand when a material will localize we must be able to accurately model its pre-localization continuum, or bulk, behavior. The bulk behavior of geomaterials is complex, and was studied at the outset of this project, with results summarized in Chapter 2 of [1] and [2]. Those results will not be repeated here, but additional discussion on plasticity models for geomaterials and their implementation may be found in [3–6].

After we understand how stresses and strains will distribute in a body, we are in a position to determine where, and in what manner, localization will initiate. Several criteria have been explored to predict localization in materials. Simple stress- or strain-based criteria have been used; for example the maximum tensile stress in concrete. Fracture mechanics has shown significant promise, provided that some information is given about the flaw size and orientation in the material. For larger continuum simulations, bifurcation theory has been widely applied. The essence of this theory is that at some points, the stress-strain relationship may become non-unique, allowing for an arbitrary strain or displacement jump in the material. Hadamard [7] was one of the pioneers of this theory, with subsequent contributions by Thomas [8], Nadai [9], and Hill [10]. The work of Rice and Rudnicki [11–13] is now considered classic for geomaterials. In the finite deformation regime, this analysis has been extended by Borja [14] and others. This work has been extended to look at instabilities related to compaction and dilatation bands [15, 16], and liquefaction [17], but this disseration will focus on shear and dilatant shear modes of localization. Another important characteristic of bifurcation theory is that once bifurcation is detected, the character of the governing partial differential equations changes, creating and boundary value problem that is ill-posed. This change can create a spurious dependence on mesh or interval size for numerical techniques.

Once localization has begun, the intense straining generally affects the mechanical properties of the materials. For quasi-brittle material like rock, concrete, and ceramics, the cohesive strength degrades to zero rapidly, typically over slip distances on the order of 0.5 mm [18]. The stress drop in this 'slip weakening' regime is approximately linear. Once the cohesion has been completely eliminated, the response in these materials is purely frictional.

The frictional response of these materials, however, is not constant. This observation

is widely recognized in the geosciences community, but is less studied in geotechnical engineering. The friction between two surfaces can vary as a function of the slip speed, temperature, fluid or gouge material on the interface, wear on a changing population of contacts, and other factors. To capture these effects, a phenomenological rate- and state- dependent friction model has been developed by Rice, Dieterich, Ruina, and others [19–22]. This model has several variations, including some that explicitly account for temperature [23, 24], which are beyond the scope of the project.

1.3 The numerical modeling of localization

Once the bulk behavior, localization condition, and post-localization response have been characterized at the constitutive level, there is still the matter of applying this knowledge to complex boundary value problems where the stresses and deformations may vary across a body. In traditional geotechnical engineering applications, so-called 'limit equilibrium' techniques have been developed to determine when a geotechnical structure might fail. While these approaches yield fairly reliable, if conservative, results for traditional applications such as slope stability problems, they leave out much of the complex physics discussed above. They also make assumptions on the shape of the failure surface and give no information about post-localization movement.

For more general problems, analytical solutions would prove quite unwieldy, especially with the complexity of the constitutive behavior involved. Hence we turn to numerical modeling techniques. While finite difference, boundary elements and host of other techniques have their benefits, the finite element method is a promising approach to this problem quite well for two reasons. First, the technique captures a wide range of geometries and loading conditions well. Second, the finite element method is one of the easiest frameworks for embedding complex constitutive properties.

As mentioned previously, however, when bifurcation occurs, the governing PDEs become ill-posed. This change in character results in a spurious mesh dependence for the method. In other words, the results become meaningless. To address this issue, two broad classes of techniques have been developed to regularize the solution. The first set of techniques add information to the equations to keep their character constant. These techniques include viscous regularization [25, 26], nonlocal [27, 28] and gradient plasticity [29–31], and Cosserat continua [32]. All of these techniques can regularize the solution. They are very promising in capturing localized deformation patterns of finite dimension, and the best of these techniques are linked to physically-based phenomena. A major drawback of these methods, however, is that they require several elements across the thickness of the band to accurately resolve the deformation. When the location of the localized region is not know *a priori*, this resolution requirement can result in meshes that are prohibitively expensive to solve computationally. The expense may be particularly acute in geotechnical and geological problems where the difference in length scales between the localized region

(millimeters to centimeters) and the problem of interest (meters or kilometers) is several orders of magnitude.

An alternative approach to this type of modeling is to approximate the localized area as a surface. Since the difference in length scales is so extreme, we can justify this approximation provided that we properly incorporate the physics of the problem onto the surface [33]. For more brittle materials, such as rock, concrete, and ceramics, the concept of a slip surface may be more appropriate already. There are at least two ways to incorporate a localized surface into a finite element framework. If the propagation path of the localized surface can be predicted, such as at a weak interface between two layers of rock, the mesh can be aligned with the path and contact elements [34, 35] or cohesive surface elements [1, 36] can be inserted along the path.

However, in many situations it is not possible to predict the orientation and path of the localized surface. For this situation, a class of finite elements have been developed that allow for a surface to be inserted at an arbitrary orientation and, in many cases, position within the element [33, 37–66]. Many of these elements also have the ability to track the propagation of the band across element boundaries in a continuous fashion. The formulation in this report follows the enhanced strain formulation of Simo and co-workers [38, 39], and more closely the reformulation of Borja and Regueiro [51–56], which is described in more detail in Section 3.3. Other sub-classes of this element type have been described and differ primarily in the way the extra degrees of freedom are condensed; see [48, 57] for reviews of the various types of these elements.

The majority of the studies with these elements, however, use relatively simple constitutive laws. Friction models with rate- and state- dependence have not been addressed. One of the key contributions of this project is the embedding of this frictional response on the slip surface. The combined constitutive response is formulated using a generalized trapezoidal scheme. One of the advantages of this scheme is that the implementation is suitable not only for the strong discontinuity element, but is readily adaptable to a variety of numerical techniques. These techniques simply must be able to determine how the shear and normal stress in the body relax with slip, which is necessary for any model with a discrete surface.

1.4 The structure of this report

The goal of this project, then, is to formulate an appropriate constitutive response for geomaterials undergoing localization and embed this model into a strong discontinuity finite element. The report has been split into two major sections. The development of the coupled slip weakening-frictional response for geomaterials is the subject of Chapter 2. Chapter 3 focuses on the formulation of an enhanced finite element capable of capturing such complex surface constitutive responses. Chapter 4 summarizes the accomplishments and suggests directions for future research.

1.5 Notation

Before continuing, it is helpful to briefly present some of the notational conventions used in the report. The summation convention, or Einstein's notation, will be used throughout the report where not explicitly stated otherwise by the note `(no sum)`. For example, $\sigma_{ii} = \sigma_{11} + \sigma_{22} + \sigma_{33}$.

Vector and tensor quantities will be written in symbolic form using boldface. Scalar quantities will not be boldface. Vector and tensor products are defined as follows: The symbol '$\cdot$' implies the contraction over the inner index of two vectors or tensors. For example, for vectors $\boldsymbol{a}$ and $\boldsymbol{b}$, $\boldsymbol{a} \cdot \boldsymbol{b} = a_i b_i$, and for second-order tensors $\boldsymbol{\alpha}$ and $\boldsymbol{\beta}$, $(\boldsymbol{\alpha} \cdot \boldsymbol{\beta})_{ij} = \alpha_{ik}\beta_{kj}$. Similarly, the symbol ':' represents the contraction of the innermost two indices of two tensor quantities. For example, $\boldsymbol{\alpha} : \boldsymbol{\beta} = \alpha_{ij}\beta_{ij}$ or $(\boldsymbol{C} : \boldsymbol{\epsilon})_{ij} = C_{ijkl}\epsilon_{kl}$. The symbol symbol '$\otimes$' denotes an outer or tensor product, with no contraction on any of the indices, such that $(\boldsymbol{a} \otimes \boldsymbol{b})_{ij} = a_i b_j$ and $(\boldsymbol{\alpha} \otimes \boldsymbol{\beta})_{ijkl} = \alpha_{ij}\beta_{kl}$.

This page intentionally left blank.

Chapter 2

Continuum Mathematical Modeling of Slip Weakening in Geological Systems

2.1 Introduction

Deformation of the Earth's crust from tectonic forces involves both diffuse elastic and plastic strains, rigid body translations and rotations, and localized deformations concentrated along narrow fault zones [67, 68]. Movement along fault zones may occur slowly by creep and/or differential slippage, as well as by sudden rupture [69, 70]. Earthquake ground motion induced by tectonic forces is interpreted to be caused by dynamic slip instability associated with rupture propagation along fault zones causing a sudden drop in shear stress [13]. The magnitude of the stress drop and the amount of slip required to realize this stress drop is quantified by the shear fracture energy and is commonly correlated with the size of an earthquake [18, 68, 71, 72].

Slip weakening is the process used to describe the strength degradation within the fault zone during the initial stage of slip instability. The concept was motivated by the cohesive zone models for tensile fracture developed by Barenblatt [73], Dugdale [74], and Bilby, et al. [75], and extended to the shear fracture problem by Ida [76] and Palmer and Rice [77]. As the Earth's crust is deformed the stress increases until it reaches a peak resistance. For intact or relatively undamaged rocks this peak resistance may consist of frictional and cohesive components along potential faults, whereas for previously faulted rocks the peak resistance may be predominantly frictional in nature, although the coefficient of friction may have increased as a result of aging of the contact. Once the peak resistance is reached intact rocks may fail by development of a new fault zone, whereas previously faulted rocks may deform by reactivation of an old fault zone or the creation of a new one depending on the current loading direction. The shear strength then decays to a lower level on those segments of the fault that slipped. This 'residual' strength is commonly interpreted to be purely frictional in nature with the coefficient of friction at the residual state being generally lower than the peak value for previously faulted rocks.

To better understand the process of slip weakening in earthquake fault zones, specimens of rocks have been tested in the laboratory and values of the shear fracture energy have been inferred from measurements [13, 18, 78–80]. While these experiments do not capture all of the processes of a fault on geologic scale, they do yield some insight into fracture and post-fracture behavior of rocks. However, the analysis of the test data is not trivial because the stress paths are different for each type of test. For example, in the biaxial tests performed by Okubo and Dieterich [79] the normal stress on the fault zone was held constant, whereas in the triaxial test results analyzed by Wong [18] and Rice [13] the normal stress was steadily decreasing during the slip weakening. Furthermore, the coefficient of friction may be changing during the slip-weakening process [19, 20], although this latter factor may have second-order effects compared to a variable normal stress which is first-order. Nevertheless, from a static equilibrium configuration to the initial activation of a fault the coefficient of friction increases rapidly from zero to a nearly steady-state value, and so within this very narrow time interval the effect of a variable coefficient of friction also could be first-order.

Construction of a slip-weakening model from compression test data on initially intact rock specimens requires transformation of post-failure data to infer the shear stress versus shear slip responses [18, 80]. A common slip-weakening law describing the degradation of shear stress on fault zones is provided by a linear function of slip with the total shear stress dropping linearly from a peak value τ° to a residual value τ^{+} over a cumulative slip ζ^{+} [76]. During the slip nucleation process the frictional resistance picks up but its exact variation remains unknown until after the segment has slipped enough for the fault to be well defined, i.e., when the slip has reached the critical value ζ^{+}. Thus, whereas the slope of the straight line can be explicitly calculated from test results after the fact, it cannot be supplied as a given parameter in the analysis of a general boundary-value problem because it is actually a state variable whose value depends on the final frictional resistance at residual state.

This chapter formulates the linear slip-weakening law implicitly by expressing the unknown frictional resistance at residual state in terms of its current value, plus some higher-order contributions arising from a Taylor series expansion. The truncated Taylor series relies on the slope of the stress path on the normal stress-shear stress (σ, τ) plane, $d\sigma/d\tau$, which is constant in conventional triaxial compression tests but could vary in a complicated way for a general 3D loading condition. For the latter case we propose an alternative simplified slip-weakening law that captures the straight line variation only in an approximate way, but does not utilize the slope $d\sigma/d\tau$. The formulation has the advantage in that the linear slip-weakening law can be captured either exactly or approximately without explicitly prescribing the slope of the line.

Experimental observations also suggest that the coefficient of friction for fault zones is a function of the slip speed and a state variable reflecting the maturity of contact [19, 20]. Therefore, the frictional resistance at the residual state must also reflect this aspect in principle. Unfortunately, incorporating velocity- and state-dependent

friction is not suitable for manual calculations because they are so involved mathematically. In the first place, the time integration can only be done numerically in most cases because of the coupling between slip velocity and the state variable. In the second place, the linearization that must be done to solve the inverse problem (i.e., given the load, find the displacement) with Newton iteration must reflect the coupling between these two variables. Therefore, we propose the use of nonlinear finite element calculations for the solution of general boundary-value problems involving faulting, as discussed in the next chapter.

The problems in this chapter analyzed quasi-statically even though rupture propagation is inherently a dynamic process. Dynamic rupture propagation, commonly encountered in earthquake fault modeling, involves fast sliding velocities and slips that are much larger than those commonly encountered in laboratory experiments. These large slips and slip rates could activate additional weakening mechanisms such as flash heating, for example, resulting in a much lower frictional resistance during dynamic sliding [81]. In such a case, the Dieterich-Ruina rate and state friction law may have to be modified to permit much stronger weakening at high slip velocities and/or large slips, see also [82]. This chapter focuses only on slow slip velocities and laboratory-derived friction laws.

2.2 Inelastic continuum modeling of rock mechanical behavior

The mechanical behavior of most rock types of interest to the earth scientist varies considerably with temperature, confining pressure, and strain rate. In order to limit the scope of this chapter, we shall restrict the discussion to rock materials tested in the laboratory at constant temperature and under a range of confining pressures that is currently supported by available testing equipment (e.g. up to around 1,000 MPa) [83]. The mechanical behavior of these materials is typically represented by a stress-strain curve that is initially linear and has a steep slope. This stage of deformation is the elastic region because when the stress is removed the original dimension of the material is recovered completely. Some rocks may suddenly fracture, or fail in brittle mode, while still deforming in the elastic regime. The value of the stress at this point is known as the brittle strength [84, 85]. If fracture creates a shear failure plane, then the ruptured material will subsequently slip along this plane. We denote the complete Cauchy stress tensor at the point of fracture by the symbol σ_{ij}°.

If the rock is not brittle, then the slope of the stress-strain curve flattens out at some point of deformation. This stage of deformation is commonly called the inelastic (or plastic) regime because when the load is removed a certain portion of deformation remains. The stress-strain curve may continue to exhibit a positive slope until eventually it reaches a certain peak stress. Typically the peak stress is accompanied by the appearance of a thin zone of shear strain localization in the sample commonly called

a shear band, although this terminology has been superseded as of late by a more general term 'deformation band' to reflect the fact that other modes of deformation, such as dilatation and compaction, may also be present in addition to shearing within the localized zone. We also denote the complete Cauchy stress tensor at the point of initial appearance of a deformation band by the same symbol σ_{ij}°. Hence, σ_{ij}° generally represents the transition stress between an intact state to a state characterized by strain localization.

For a general three-dimensional loading condition the elastic region is assumed to be bounded by a so-called yield surface defined by the equation

$$F(\sigma_{ij}, \kappa) = 0 \tag{2.1}$$

where σ_{ij} is the symmetric Cauchy stress tensor and κ is a plastic variable describing the extent of the elastic region. Since plastic yielding reflects a material's constitutive behavior, the yield surface should not depend on the reference frame (i.e, it is frame-invariant). For more details on plasticity models for geomaterials, the reader is again referred such references as [1–6].

The onset of a shear band in an intact rock signifies the end of a homogeneous deformation response. Viewed as a material instability, shear bands had been investigated in the past based on the works of Hadamard [7], Hill [10], Thomas [8] and Mandel [86] within the context of acceleration waves in solids. For geological materials, Rudnicki and Rice [11] presented a condition for the onset of a shear band, embodied by the classical equation

$$\det(\boldsymbol{Q}) = 0\,, \qquad Q_{ik} = n_j c_{ijkl}^{\mathrm{ep}} n_l \tag{2.2}$$

where c_{ijkl}^{ep} is the rank-four elastoplastic constitutive operator; and n_j and n_k define components of the unit normal vector $\boldsymbol{n}$ to the band. The rank-two tensor $\boldsymbol{Q}$ is known in the literature as the acoustic tensor, and the determinant of this tensor as the localization function.

The localization function is assumed to be initially positive for any orientation $\boldsymbol{n}$. As the material deforms and its stiffness degrades, the value of the localization function decreases. At a certain point in the loading history where the localization function crosses the value zero, bifurcation into a shear band occurs, and the orientation of the emerging shear band is described by the vector $\boldsymbol{n}$. Because the material is yielding at this particular point of deformation, the stress point is instantaneously on the yield surface, and so we have

$$F(\sigma_{ij}^{\circ}, \kappa^{\circ}) = 0 \tag{2.3}$$

where κ° defines the size of the elastic region at the point of bifurcation, and σ_{ij}° is the bifurcation stress.

2.3 Formulation of slip-weakening model: linear and simplified laws

We assume that the slip surface is defined by a unit normal vector $\boldsymbol{n}$ (with components n_i). If σ_{ij} is the continuum stress tensor, then the resolved normal and tangential shear stresses (σ and τ, respectively) on the slip surface may be calculated as

$$\sigma = \sigma_{ij} n_i n_j \,, \qquad \tau = \sqrt{t_i t_i} \,, \qquad t_i = \sigma_{ij} n_j - \sigma n_i \tag{2.4}$$

Here we have used the strength of materials convention for the Cauchy stress where a normal stress component is positive under tension. For later use we define the stress path on the σ-τ plane by the slope

$$\frac{\delta\sigma}{\delta\tau} = \frac{n_i n_j \delta\sigma_{ij}}{\xi_{km}\delta\sigma_{km}} \,, \qquad \delta\tau \neq 0 \tag{2.5}$$

where

$$\xi_{km} = \frac{1}{2}(l_k n_m + l_m n_k) \,, \qquad l_k = t_k/\tau \tag{2.6}$$

We identify l_k as a component of a (normalized) unit traction vector tangent to the slip surface. In the above expression for the stress path we assume that deformations are sufficiently small so that the orientation vector $\boldsymbol{n}$ for the slip surface may be considered essentially constant during the slip weakening. Furthermore, the case $\delta\tau = 0$ is simply a "horizontal" stress path.

Next we define the slip velocity vector as

$$[\![\boldsymbol{v}]\!] = \dot{\zeta}\boldsymbol{m} \tag{2.7}$$

where $\boldsymbol{m}$ is a unit vector in the direction of slip, and $\dot{\zeta}$ is the magnitude of the slip rate. For shear fractures, $\boldsymbol{m}$ is typically tangent to the slip surface although some minor variations may be observed on a smaller scale depending on the interaction of comminuted particles with the slip surface. The cumulative slip is defined by the integral

$$\zeta = \int_t \dot{\zeta} \, \mathrm{d}t \tag{2.8}$$

where the integration is taken over the slip path.

To make the above equations more physically meaningful, we consider an initially intact rock sample subjected to triaxial loading with σ_1, σ_2, and σ_3 representing the major, intermediate, and minor compressive principal stresses, respectively, as shown in Fig. 2.1a. All of these principal stresses act on the faces of the specimen, with σ_2 representing the out-of-plane normal stress. A slip surface forms on the plane defined by σ_1 and σ_3 and inclined at an angle ϑ relative to σ_1. The normal and shear stresses on the slip plane are given by

$$\sigma = \sigma_1 \sin^2\vartheta + \sigma_3 \cos^2\vartheta \,, \qquad \tau = \frac{1}{2}(\sigma_3 - \sigma_1)\sin 2\vartheta \tag{2.9}$$

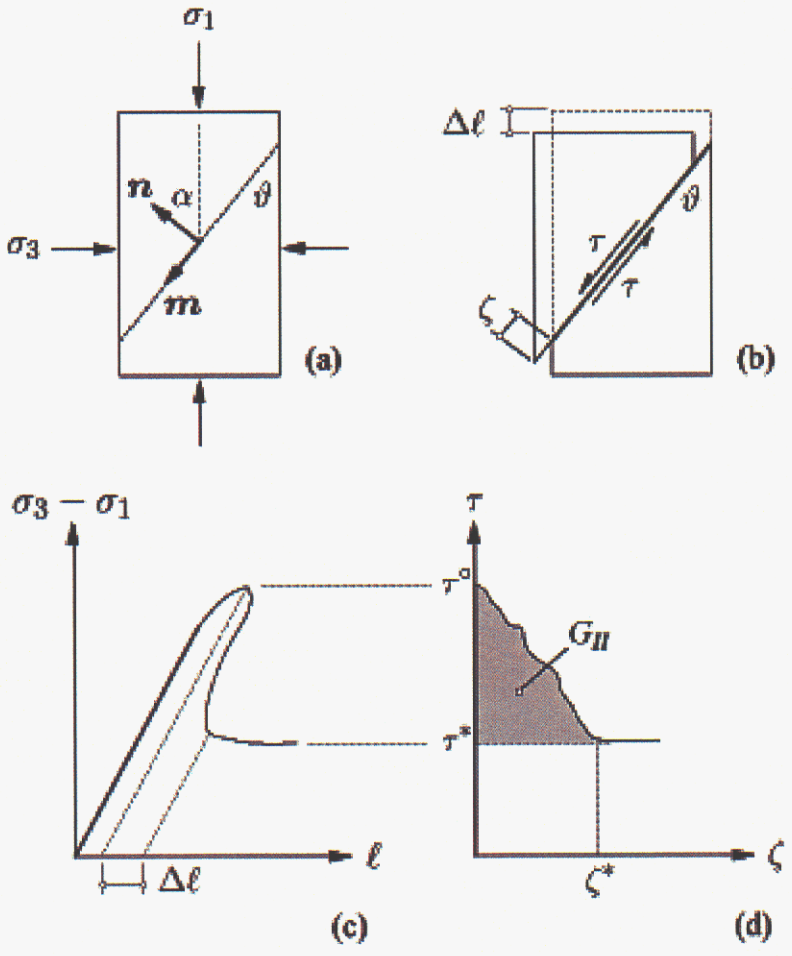

Figure 2.1: Shear strain localization of an initially intact rock sample: (a) condition at localization; (b) post-localization defining relative slip assuming rigid shearing bodies; (c) global stress-compression response of sample; (d) inferred slip-weakening response (after [87]).

During the slip weakening the compressive stress σ_1 is reduced while σ_3 remains fixed; hence the stress path is given by the constant slope

$$\frac{\delta\sigma}{\delta\tau} = -\frac{2\sin^2\vartheta}{\sin 2\vartheta} = -\tan\vartheta \tag{2.10}$$

On the other hand, Fig. 2.1b shows that if the sliding blocks are relatively rigid the slip ζ can be related to the incremental axial shortening $\Delta\ell$ according to the approximate relation

$$\zeta = \Delta\ell/\cos\vartheta \tag{2.11}$$

As the slip ζ builds up the resolved shear stress τ decreases until it reaches a steady-state value called the residual shear stress τ^+ when the slip has reached the critical value ζ^+. We are interested in developing a slip-weakening constitutive law describing the reduction of shear stress τ with slip over the region $\zeta \in [0, \zeta^+]$.

Figures 2.1c,d demonstrate how to transform the stress-displacement test data to infer the post-localization τ-ζ response (see [18, 80]). The overall specimen response depicted in Fig. 2.1c represents a class I behavior in which the maximum principal stress difference decreases so dramatically at post-localization, assumed in the figure to occur at the peak point, that the stress-displacement curve turns over so far as to follow a positive slope [87, 88]. This is in contrast to a more regular class II stress drop with a negative slope. Assuming that the elastic Young's modulus remains constant during the test, then $\Delta\ell$ at post-localization is calculated as shown in Fig. 2.1c, and the shear strength-slip displacement curve may be constructed as shown in Fig. 2.1d.

The shear stress-slip curve shown in Fig. 2.1d has a peak value of τ° at the beginning of the slip weakening. The shear strength mobilized on the slip plane then decreases until it stabilizes to a residual value τ^+ when the slip has reached a value approximately equal to $\zeta^+ \approx 0.5$ mm for most rocks [18]. Thereafter, the shear stress remains essentially constant at this residual value. By comparison, Ohnaka et al. [89] presented a shear stress-slip curve for faulting in an initially intact rock with the shear stress first increasing to a peak value at "apparent" slip displacement equal to D_a, then dropping to the residual value at ζ^+. The Ohnaka et al. curve was obtained by subtracting the linear elastic response but not the bulk plastic response prior to localization, and so in principle their peak stress takes the same meaning as the stress τ° used in the present chapter. Although the slip-weakening curve may exhibit some slight irregularities, a linear slip-weakening law is usually assumed and takes the form [76, 90–92]

$$\tau_f = \tau^\circ - (\tau^\circ - \tau^+)\frac{\zeta}{\zeta^+}, \qquad \zeta \in [0, \zeta^+] \tag{2.12}$$

This law satisfies the essential conditions $\tau_f = \tau^\circ$ at $\zeta = 0$, and $\tau_f = \tau^+$ at $\zeta = \zeta^+$. The given parameters are τ°, which we determine from (2.4) at the transition stress σ°_{ij}, and the critical slip distance ζ^+.

The problem with equation (2.12) is that neither the residual shear stress τ^+ nor the slope $-(\tau^\circ - \tau^+)/\zeta^+$ is known since the constitutive properties of the slip surface as well as the normal stress acting on this surface may be changing during the slip weakening process. Hence, it is not possible to compute the total stress drop $\Delta\tau = \tau^\circ - \tau^+$ until after the residual shear stress has already been calculated. On the other hand, the residual shear stress τ^+ in rock faults arises only from pure friction, so if we assume a coefficient of friction on the slip surface μ then the frictional shear resistance is $f = -\mu\sigma$, and hence $\tau^+ = f^+ = -\mu^+\sigma^+$. The current value of f is always known during the slip weakening process, so our objective is then to express f^+ in terms of the known value of the frictional shear stress f. The key point here is to treat the slope $-\Delta\tau/\zeta^+$ implicitly, rather than explicitly, as demonstrated below.

Expanding f^+ about f using the Taylor series expansion gives

$$\tau^+ = f^+ = f + \frac{\partial f}{\partial \zeta}(\zeta^+ - \zeta) + \frac{1}{2!}\frac{\partial^2 f}{\partial \zeta^2}(\zeta^+ - \zeta)^2 + \dots \tag{2.13}$$

$$\approx f + \frac{\partial f}{\partial \zeta}(\zeta^+ - \zeta) \tag{2.14}$$

where we have ignored the terms in the Taylor series involving the second and higher derivatives. The coefficient of friction μ may also depend on the slip rate, as elaborated further in the next section, but its effect is usually second-order in comparison to that of a variable σ, so ignoring the variation of μ we simply write

$$\frac{\partial f}{\partial \zeta} = -\mu \frac{\partial \sigma}{\partial \zeta} = -\mu \frac{d\sigma}{d\tau}\frac{\partial \tau}{\partial \zeta} \tag{2.15}$$

where $d\sigma/d\tau$ is the slope of the stress path given by equation (2.5) for a general 3D continuum loading. For continued slip weakening $\tau = \tau_{\mathrm{f}}$, so imposing the linear slip weakening law we get

$$\frac{\partial f}{\partial \zeta} = -\mu \frac{d\sigma}{d\tau}\frac{\partial \tau_{\mathrm{f}}}{\partial \zeta} = -\mu \frac{d\sigma}{d\tau}\left(\frac{\tau_{\mathrm{f}} - \tau^\circ}{\zeta}\right), \qquad \zeta \neq 0 \tag{2.16}$$

where the quantity inside the parentheses represents the constant slope $\partial \tau_{\mathrm{f}}/\partial \zeta$ implied by the linear slip-weakening constitutive law, see Fig. 2.2. Note that this slope is also equal to $(\tau^+ - \tau^\circ)/\zeta^+$, as shown in Fig. 2.2, but as noted before τ^+ is yet to be calculated so this latter expression cannot be used.

Substituting this result into (2.14) yields

$$\tau^+ = f - \mu \frac{d\sigma}{d\tau}\left(\frac{\tau_{\mathrm{f}} - \tau^\circ}{\zeta}\right)(\zeta^+ - \zeta), \qquad \zeta \neq 0 \tag{2.17}$$

The above expression depends only on the current state variables ζ, f, τ_{f}, and the slope $d\sigma/d\tau$. Inserting this expression into the linear slip-weakening constitutive law (2.12) then gives

$$\tau_{\mathrm{f}} = \chi^{-1}\tau^\circ(1-\eta)\left(1 + \mu \frac{d\sigma}{d\tau}\right) + \chi^{-1} f \eta \tag{2.18}$$

where

$$\chi = 1 + \mu(1-\eta)\frac{d\sigma}{d\tau}, \qquad \eta = \zeta/\zeta^+ \tag{2.19}$$

Like equation (2.12), equation (2.18) also satisfies the conditions $\tau_{\mathrm{f}} = \tau^\circ$ at $\eta = 0$, and $\tau_{\mathrm{f}} = f^+$ at $\eta = 1$.

To elucidate the above slip-weakening law, we consider a triaxial compression test reported by Wong [80] on Sample G3 of San Marcos gabbro. The test was conducted by varying the major compressive stress σ_1 while holding σ_2 and σ_3 fixed. Assuming

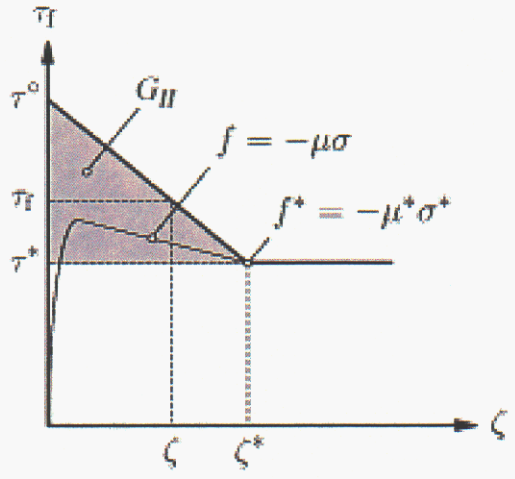

Figure 2.2: Graphical representation of linear slip weakening: as shear stress weakens linearly to residual value, frictional resistance picks up while cohesion decays to zero. The shear fracture energy is represented by the shaded area of triangle.

the principal stress directions remained fixed during the test, the instantaneous stress path is given by the slope $d\sigma/d\tau = -\tan\vartheta$, where the physical significance of ϑ is shown in Fig. 2.1. Wong [80] reported a confining stress $\sigma_3 = -250$ MPa, which was held constant during the test. At peak, the stresses were $\tau^\circ = 433$ MPa and $\sigma^\circ = -500$ MPa; at residual, they were $\tau^+ = 326$ MPa and $\sigma^+ = -439$ MPa. We back-figure the coefficient of friction at residual state to be $\mu^+ = -\tau^+/\sigma^+ = 0.743$, which we assumed constant in the present analysis. The total drops in the normal and shear stresses were $\Delta\sigma = \sigma^+ - \sigma^\circ = 61$ MPa and $\Delta\tau = \tau^+ - \tau^\circ = -107$ MPa, respectively, and so from (2.10) we calculated $\vartheta = \tan^{-1}(-\Delta\sigma/\Delta\tau) = 30°$. This agrees with a reported angle of $\alpha = 90° - \vartheta = 60°$ in Table 1 of [80], see Fig. 2.1a for the physical significance of the angle α.

Now we use equation (2.18) to predict the slip-weakening response. First, we substitute $d\sigma/d\tau = -\tan\vartheta$ into (2.18) and (2.19). Since the material is slipping continually, $\tau_f = \tau$. Inserting (2.9) into the expressions for $f = -\mu\sigma$ and τ, and ignoring the variation of μ, we obtain the expected variation of σ_1 during this test as follows:

$$\sigma_1 = \frac{\sigma_3[\,\mu\eta\cos^2\vartheta + (\chi\sin 2\vartheta)/2\,] - \tau^\circ(1-\eta)(1-\mu\tan\vartheta)}{(\chi\sin 2\vartheta)/2 - \mu\eta\sin^2\vartheta} \tag{2.20}$$

$$= \sigma_3\Big[\,1 + \frac{2\mu}{(1-\mu\tan\vartheta)\sin 2\vartheta}\eta\,\Big] - \frac{2\tau^\circ}{\sin 2\vartheta}(1-\eta) \tag{2.21}$$

where $\chi = 1 - \mu(1 - \eta)\tan\vartheta$. The second line of equation (2.21) describes a linear drop of σ_1 with $\eta = \zeta/\zeta^+$. That we recover a linear drop exactly is hardly surprising since τ is postulated to drop linearly with η, so σ will also drop linearly since we assumed a constant coefficient of friction μ and $d\sigma/d\tau$ is constant. This implies that f will also vary linearly with η, and so only the first derivative of f in the Taylor series is needed to determine the exact residual value f^+.

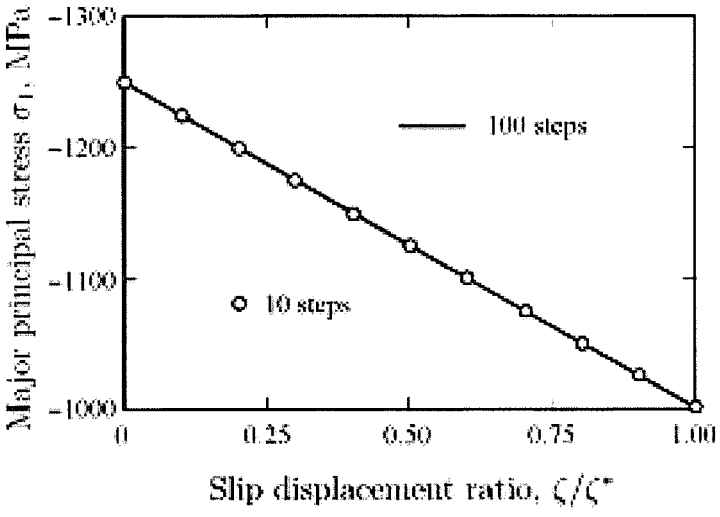

Figure 2.3: Linear drop of major principal stress during triaxial testing of San Marcos gabbro (Sample G3) manifested by 10 and 100 load step solutions. The two solutions are identical to machine precision.

Figure 2.3 shows a plot of equation (2.21) for Sample G3 of San Marcos gabbro. For this simulation, ten- and 100-increment solutions were performed and the predicted variation of σ_1 is perfectly linear for either case. We emphasize that the calculations shown in Fig. 2.3 did not make use of the residual shear stress τ^+ even though this information was provided by Wong [80]. In fact, substituting (2.21) into the expression for τ in (2.9) gives the following linear slip weakening constitutive law for the triaxial compression test performed by Wong:

$$\tau_{\rm f} = \tau^\circ(1 - \eta) - \frac{\mu\sigma_3}{1 - \mu\tan\vartheta}\,\eta \tag{2.22}$$

Again, this equation meets both end conditions with $\tau_{\rm f} = \tau^\circ$ at $\eta = 0$, and $\tau_{\rm f} = -\mu\sigma^+$ at $\eta = 1$ after noting that $\sigma^+ = \sigma_3/(1 - \mu\tan\vartheta)$ for σ_1 obeying (2.21). For completeness we show in Fig. 2.4 a 3D plot in the $(\zeta, f, \tau_{\rm f})$ space of equation (2.18) for this test.

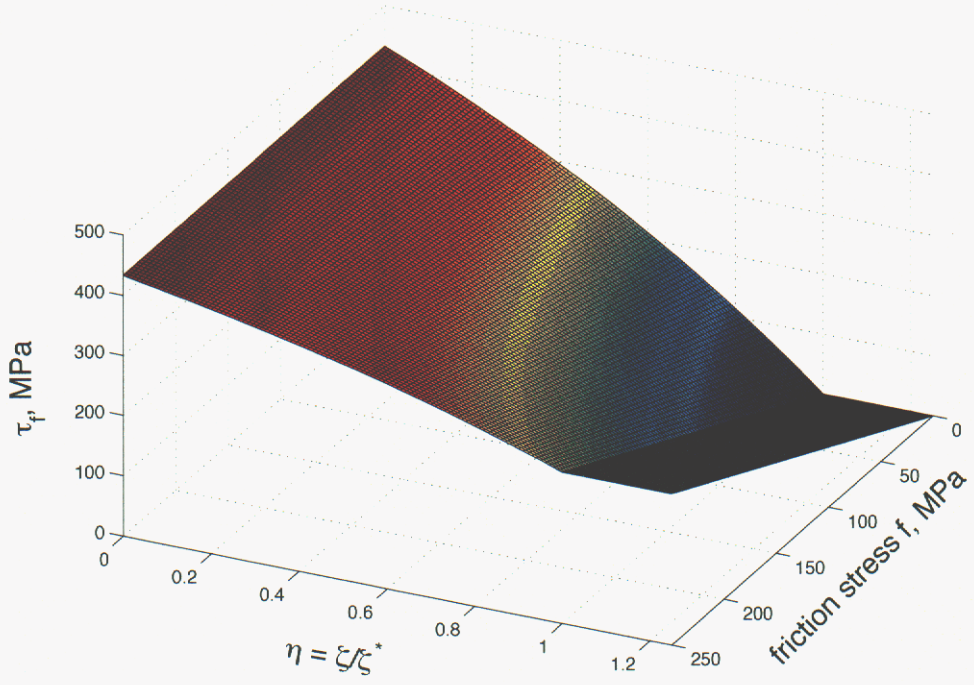

Figure 2.4: Predicted drop of major principal stress during triaxial testing of San Marcos gabbro (Sample G3). The simplified law is concave downwards relative to the linear law since f decreases during slip weakening for this test.

For a general boundary-value problem equation (2.18) requires the evaluation of the slope $d\sigma/d\tau$ of the stress path, which could make the calculations unwieldy. For the triaxial test example described above this slope was constant, but in a general 3D continuum problem this slope is expected to vary in an unpredictable way. Furthermore, if the motion of the continuum is large so as to alter the orientation of the slip surface, then even the unit vector $\boldsymbol{n}$ is expected to vary, thus making the evaluation of the slope $d\sigma/d\tau$ very cumbersome. To alleviate this difficulty, we drop the first derivative in the Taylor series altogether and simply write $\tau^+ \approx f$. This leads to a simplified slip-weakening constitutive law of the form

$$\tau_{\mathrm{f}} = \tau^\circ - (\tau^\circ - f)\frac{\zeta}{\zeta^+} \tag{2.23}$$

This equation is simpler than (2.18); however, it does not recover completely the linear slip-weakening law since the Taylor series expansion was short by one term. On the other hand, equation (3.18) still satisfies the two essential end conditions at τ° and $\tau^+ = f^+$. Hence, under normal conditions we expect the deviation of (2.23) from a linear constitutive law to be 'mild.'

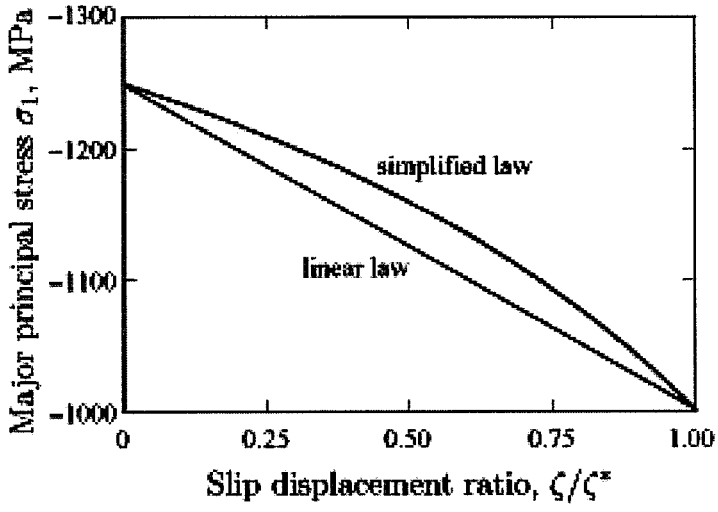

Figure 2.5: Predicted drop of major principal stress during triaxial testing of San Marcos gabbro (Sample G3). The simplified law is concave downwards relative to the linear law since f decreases during slip weakening for this test.

Repeating the analysis of the previous example, we set $\tau_f = \tau$ and $f = -\mu\sigma$, and again substitute equation (2.9) into the simplified law (2.23) to obtain the expected drop of σ_1 with slip for Sample G3 of San Marcos gabbro as follows:

$$\sigma_1 = \frac{\sigma_3[\,\mu\eta\cos^2\vartheta + (\sin 2\vartheta)/2\,] - \tau^\circ(1-\eta)}{(\sin 2\vartheta)/2 - \mu\eta\sin^2\vartheta}, \qquad \eta = \zeta/\zeta^+ \tag{2.24}$$

Figure 2.5 compares the simplified slip-weakening relation (2.23) with the linear law and suggests that σ_1 drops more slowly in the beginning but catches up toward the end as the slip reaches the critical value ζ^+. The shear fracture energy, represented in Fig. 2.1d by the shaded area and denoted by the symbol G_{II}, is thus over-predicted by about 15% relative to that computed with the linear law. Figure 2.6 shows a three-dimensional plot of (2.23) in the (ζ, f, τ_f) space and defines a warped surface. It suggests that if f increases (alternatively, decreases) during the slip weakening, then the projection of the state path on the (τ_f, ζ) plane is slightly concave upwards (alternatively, downwards). The deviation from the linear law depends on how drastically the normal stress σ varies during the slip weakening. Interestingly, Ida [76] also considered similar nonlinear slip-weakening laws exhibiting upward and downward concavities relative to the linear law.

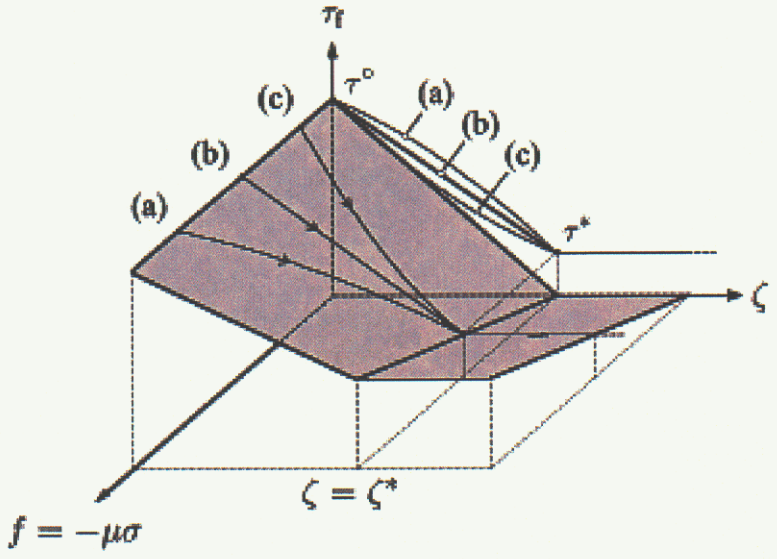

Figure 2.6: Graphical representation of simplified slip-weakening function: (a) f decreasing; (b) f constant; (c) f increasing.

2.4 Variable friction model

Figure 2.7 represents pictorially the slip-weakening process on the deviatoric plane. We assume here that the slip surface is triggered by a shear band-type bifurcation, so the transition stress σ_{ij}° lies on the yield surface $F(\sigma_{ij}^\circ, \kappa^\circ) = 0$. The figure shows two cross-sections of a conical three-invariant yield surface, one cutting through a plane $\sigma_1 + \sigma_2 + \sigma_3 = \sigma_{ii}^\circ = C < 0$ (light curve) at the point of bifurcation, and a second cutting through the π-plane defined by the equation $\sigma_1 + \sigma_2 + \sigma_3 = 0$ (heavy curve). The stress paths are all projected to the π-plane. We assume that the initial shear resistance acting on the emerging shear band is of the Mohr-Coulomb type,

$$\tau_f = c - \mu\sigma \tag{2.25}$$

where c is cohesion. At the bifurcation stress the shear stress on the band is $\tau^\circ = c^\circ - \mu^\circ\sigma^\circ$, while at the residual state a purely frictional resistance gives $\tau^+ = -\mu^+\sigma^+$. During the slip weakening the cohesive resistance dies out to zero while the frictional resistance picks up. This feature is also manifested in Fig. 2.2 which further shows that this frictional resistance generally could vary during the slip weakening process in an unpredictable way. This interplay between the two types of resistance is represented in Fig. 2.7 by the changing slopes of lines representing equation (2.25). In this section we provide an in-depth look into this interplay between the two types of resistance in a more quantitative way.

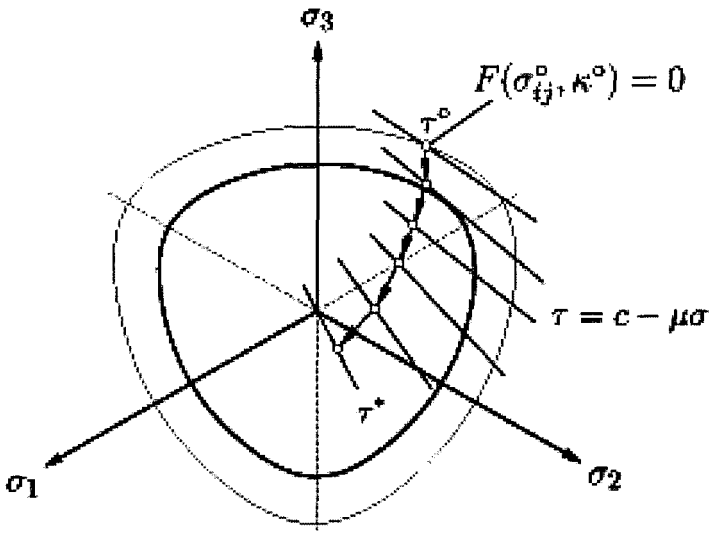

Figure 2.7: Pictorial representation of slip weakening on the π-plane. Fan of straight lines represents the Mohr-Coulomb failure criterion for a planar fault; at residual state the cohesion decays to zero, hence the failure criterion passes through the origin.

Early experimental observations suggest that the coefficient of friction μ mobilized on the surface of discontinuity between two contacting bodies subjected to a slowly increasing load is a function of the slip speed $\dot{\zeta}$ and a state variable θ reflecting the maturity of the contact. Under conditions of fixed temperature an empirical law of the following form has been proposed by Dieterich [19], Ruina [20], and Dieterich and Linker [21],

$$\mu = \mu_0 + A \ln\left(\frac{\dot{\zeta}}{V^*}\right) + B \ln\left(\frac{\theta}{\theta^*}\right) \tag{2.26}$$

where μ_0, A, and B are experimentally determined constants, and V^* and θ^* are normalizing constants. For rocks typical values of A and B range from 0.005 to 0.015.

The variation of μ in an ideal velocity stepping test is depicted in Fig. 2.8. As the velocity increases instantaneously from $\dot{\zeta}_1$ to $\dot{\zeta}_2$, the coefficient of friction increases instantaneously by an amount $A \ln(\dot{\zeta}_2/\dot{\zeta}_1)$. This momentary increase is followed by a decrease over a characteristic sliding displacement D_c , a material parameter, required to stabilize friction. The parameter D_c may be interpreted as the characteristic slip required to replace a contact population representative of a previous sliding condition with a contact population created under a new sliding condition; it may be approximated as the mean contact diameter on the order of 10 μm [93]. The role of θ is to

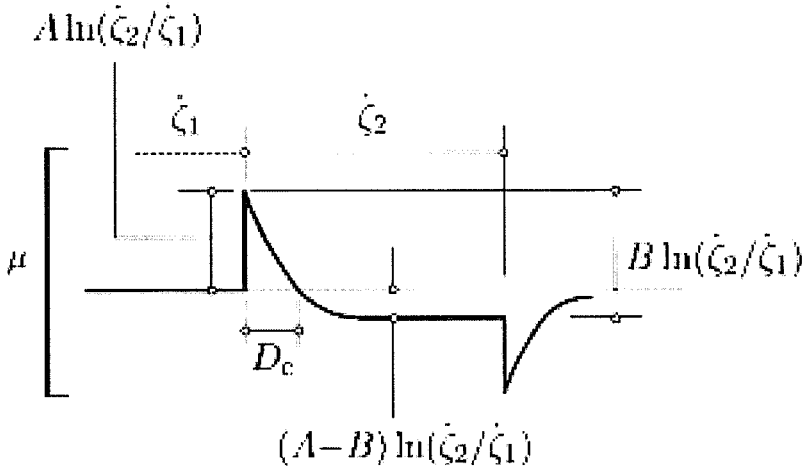

Figure 2.8: Coefficient of friction of the rate- and state-dependent friction model as it undergoes an instantaneous velocity increase, and then an instantaneous decrease.

reflect contact aging, or lifetime. An empirical evolution equation for θ first proposed by Ruina [20] takes the form

$$\frac{d\theta}{dt} = 1 - \frac{\theta\dot{\zeta}}{D_c} \tag{2.27}$$

This law allows for friction hardening of the material over time and is known as the healing form of the evolution equation. If $\dot{\zeta} = 0$, then (2.27) indicates that θ increases by an amount equal to the elapsed time of stationary contact, reflecting contact aging. If $d\theta/dt = 0$, then the steady-state value of θ is $\theta_{ss} = D_c/\dot{\zeta}$. Substituting this value in (2.26) gives

$$\mu_{ss}|_{\dot{\zeta}_1} = \mu_{ss}|_{\dot{\zeta}_2} + (A - B)\ln\left(\frac{\dot{\zeta}_2}{\dot{\zeta}_1}\right) \tag{2.28}$$

If the requirement that steady-state friction decreasing with slip speed is imposed, then the relation $A < B$ must hold [20, 94].

A drawback of the logarithmic form of friction law is that this expression is singular when the slip velocity is zero. Hence, it cannot be used to describe what occurs during initiation of a slip surface. Although based solely on empirical observations, this expression, however, has a theoretical basis if one considers friction sliding as a rate process [23, 92, 95, 96]. By doing so, one can add terms related to the possibility of random backward jumps [97, 98], resulting in

$$\mu = A\sinh^{-1}\left\{\frac{\dot{\zeta}}{2V^*}\exp\left[\frac{\mu_0}{A} + \frac{B}{A}\ln\left(\frac{\theta}{\theta^*}\right)\right]\right\} \tag{2.29}$$

This regularized form for μ has been used by Rice and Ben-Zion [22] and Ben-Zion and Rice [98]. Equation (2.29) may be combined with the evolution law for θ given by (2.27) to obtain a direct constitutive law between μ and $\dot{\zeta}$, eliminating θ as an

independent variable in the process. This may be done either analytically or numerically.

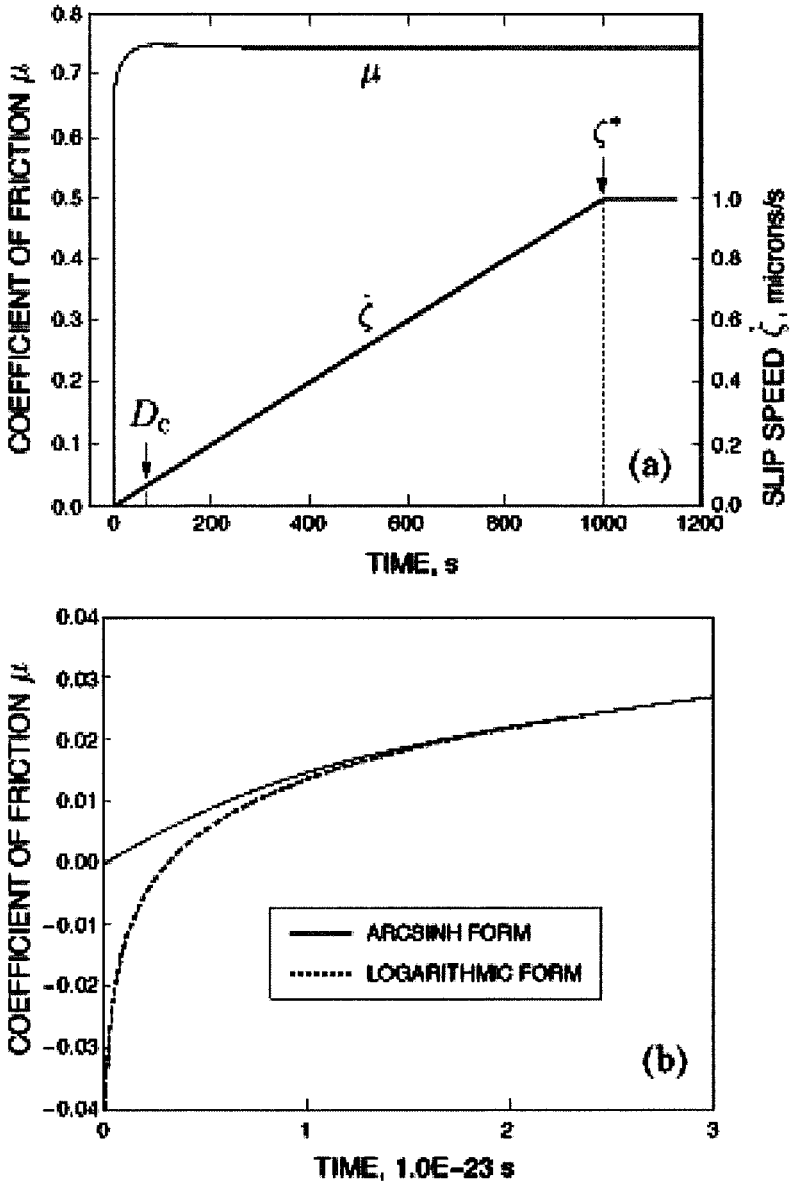

Figure 2.9: Variation of coefficient of friction: (a) variation during slip weakening; (b) comparison between arcsinh and logarithmic functions.

Figure 2.9 compares expressions (2.26) and (2.29) for Sample G3 of San Marcos gabbro analyzed earlier. To make the comparison, these two expressions were combined with Ruina's healing law (2.27) and solved numerically by trapezoidal integration.

The material parameters used were $A = 0.012$, $B = 0.0135$, $D_c = 2.25$ microns, $\mu_0 = 0.743$, $V^* = 1$ μm/s, and $\theta^* = 2.25$. The value of μ_0 was selected so that at a slip speed of 1 μm/s we recover the steady-state coefficient of friction of 0.743 (see Sec. 2.3); otherwise, the remaining parameters were taken from fits to experimental data for a granite [99]. Note that for the most part the two expressions for μ result in curves that lie one on top of the other except at extremely small slip displacements (near-zero velocity) where expression (2.26) becomes singular.

As noted in equation (2.15) the variation in μ is second-order compared to the variation of the normal stress (except at very small slip displacements on the order $\zeta < D_c$), so the linear slip-weakening form (2.18) holds even for a variable coefficient of friction. Combining this with (2.25) yields an expression for cohesion of the form

$$c = \chi^{-1}\tau^\circ(1-\eta)\Big(1+\mu\frac{d\sigma}{d\tau}\Big) + \chi^{-1}f\eta + \mu\sigma \tag{2.30}$$

where χ is given in equation (2.19). On the other hand, if we use the simplified slip-weakening law (2.23), then we get the following evolution for c:

$$c = \tau^\circ - (\tau^\circ - f)\frac{\zeta}{\zeta^+} + \mu\sigma = (\tau^\circ + \mu\sigma)\Big(1 - \frac{\zeta}{\zeta^+}\Big) \tag{2.31}$$

In either case, as the frictional resistance picks up the cohesion c inherits the 'softening' character of τ_f since it is simply equal to τ_f translated by the distance $\mu\sigma$.

2.5 Conclusions

We have presented a framework for mathematical modeling of slip weakening in an initially intact rock due to shear strain localization along any arbitrary slip plane. The framework includes a closed-form expression for a linear evolution of shear stress with slip up until the full development of a fault, given the stress path on the normal stress-shear stress plane for this fault. The formulation also includes a variable coefficient of friction, which can be implemented into a finite element framework using an embedded strong discontinuity approach, as discussed in the next chapter. The finite element model may be used not only to analyze rock test data but also to simulate faulting of the Earth's crust on a much larger scale. Work is underway to incorporate dynamic slip instability associated with rupture propagation along fault zones to better understand the influence of tectonic forces and fault properties on the ensuing seismic ground motion. Work is also underway to augment the capabilities of the element to include opening degrees of freedom to properly model local areas of tension as well as curvature along a fault.

This page intentionally left blank.

Chapter 3

Embedded strong discontinuity finite elements for fractured geomaterials with variable friction

3.1 Introduction

Strain localization, characterized by intense deformation across a narrow region, plays an important role in the behavior of many solid materials. Examples include necking and shear banding in metals, shear banding in soils, and fracturing in rocks and concrete. In addition to potentially significant displacements, an associated rapid loss of strength makes strain localization an important area of study, as this loss of strength can lead to structural failure or other unstable behaviors.

In quasi-brittle materials like many rocks, concretes, frozen soils, and heavily over-consolidated clays, strain localization often takes the form of fractured surface in the body. Kinematically, this surface is represented by a jump in the displacement field, and is termed a 'strong discontinuity.' This type of strain localization is distinct from a localized region of finite thickness, such as a shear band forming in dense sands that can be a few grain diameters thick. A localized region of finite thickness may have a jump in the strain field, or 'weak discontinuity,' but the displacement field remains continuous. It has been suggested [33, 100] that a strong discontinuity may be used to approximate a weak discontinuity provided that the physics of the band can be properly incorporated onto the surface [33]. This paper will focus on the strong discontinuity case. Although a framework for a general constitutive model will be discussed, we will not attempt to derive a constitutive model appropriate for weak discontinuities in this report.

Because the location and propagation path of a slip surface or region may be difficult to determine for complex geotechnical structures, one often uses the finite element method to analyze these problems. However, while standard finite element methods have proven useful for a wide variety of geometries, loading, and deformation patterns, modeling localized deformation using standard elements is difficult and can lead to inaccurate results. Classical associative and non-associative plasticity models could

lead to non-unique strain rate fields [11, 16], requiring a special treatment of the local bifurcation and accompanying strain localization that typically cuts through and across the finite element.

To create a stable solution and capture the anisotropic damage and movement on the fracture surfaces, we turn to a finite element that can be enhanced by inserting a surface at an arbitrary orientation and location, and allowing a displacement jump across that surface. The element employed was developed by Simo and coworkers [38, 39], and follows the recent reformulation by Borja and Regueiro [51–56]. These works, however, assumed a constant coefficient of friction along the slip surface.

The main contribution of this chapter is the incorporation of a variable coefficient of friction into the strong discontinuity formulation. A variable coefficient of friction is atypical in computational mechanics literature where a constant coefficient of friction is almost always assumed. However, it is widely recognized in geophysics and in many branches of geoscience that the coefficient of friction may depend not only on slip speed but also on a state parameter representing the maturity of contact. Thus, it cannot be assumed to be constant for important applications such as earthquake fault rupture processes. In this chapter we focus on a velocity- and state-dependent coefficient of friction applicable to slow slip velocities and laboratory-derived state and friction laws, along with the strong discontinuity finite element formulation.

The remainder of this chapter is structured as follows: We briefly review in Section 3.2 the kinematical assumptions for a strong discontinuity in the context of small strain deformation and the resulting bifurcation condition. In Section 3.3, we present the framework for enhanced strain element and its implementation. We present the numerical formulation for determining the slip in Section 3.4, and the resulting consistent stiffness formulation in Section 3.5. Numerical examples and concluding remarks close out the chapter.

3.2 Kinematics

As a point of departure, we examine kinematics that include a strong discontinuity. For the purposes of this chapter, we will use small strain assumptions. Strong discontinuity kinematics in a finite deformation setting are described in more detail in [56] and [40].

Consider a body with an otherwise smooth displacement field that contains a displacement jump across the surface S in the body. In other words

$$\boldsymbol{u} = \bar{\boldsymbol{u}} + [\![\boldsymbol{u}]\!] H_S \tag{3.1}$$

$$= \bar{\boldsymbol{u}} + \zeta \boldsymbol{m} H_S \tag{3.2}$$

where H_S is a Heaviside function across S. The vector $\bar{\boldsymbol{u}}$ is referred to as the regular part of the displacement, while $[\![\boldsymbol{u}]\!]H_S$ is the displacement jump. The magnitude of the jump is ζ, in the direction $\boldsymbol{m}$. In granular materials, dilatation on cracks is observed due to asperity mismatch and the formation of gouge material, and has been shown to have important impacts on crack behavior [101]. Hence, the slip direction is expected to not be exactly perpendicular to the normal to the slip surface. As slip continues, however, there is less further dilatation, and $\boldsymbol{m}$ becomes closer to parallel to being the band.

In the infinitesimal regime, the strain field becomes

$$\boldsymbol{\epsilon} = \nabla^s \boldsymbol{u} = \nabla^s \bar{\boldsymbol{u}} + \nabla^s \left(\zeta \boldsymbol{m}\right) H_S + \zeta \left(\boldsymbol{m} \otimes \boldsymbol{n}\right)^s \delta_S \tag{3.3}$$

with $\boldsymbol{n}$ as the normal to S, δ_S the Dirac delta distribution across S, and $(\bullet)^s$ denoting the symmetric part of the tensor $(\bullet)$. The spatial gradient of the jump will generally be quite small compared to the jump itself. In the finite element approximation, we consider the jumps to be constant within a given element, so the second term disappears, leaving

$$\boldsymbol{\epsilon} = \nabla^s \boldsymbol{u} = \nabla^s \bar{\boldsymbol{u}} + \zeta \left(\boldsymbol{m} \otimes \boldsymbol{n}\right)^s \delta_S \tag{3.4}$$

For the finite element formulation, it is convenient to reformulate the displacement field as

$$\begin{aligned} \boldsymbol{u} &= \tilde{\boldsymbol{u}} + \hat{\boldsymbol{u}} && (3.5)\\ &= \tilde{\boldsymbol{u}} + [\![\boldsymbol{u}]\!] M_S && (3.6)\\ &= \left(\bar{\boldsymbol{u}} + f^h [\![\boldsymbol{u}]\!]\right) + [\![\boldsymbol{u}]\!] \left(H_S - f^h\right) && (3.7) \end{aligned}$$

Here f^h is an arbitrary smooth function that is equal to zero at all the element nodes on the "passive" side of the element, where $H_S = 0$, and unity at all the nodes on the "active" side, where $H_S = 1$.

We use a convenient and typical form for f^h, the sum of the shape functions of the active nodes

$$f^h = \sum_{A=1}^{n_{en}} N_A H_S \left(\boldsymbol{x}_A\right) \tag{3.8}$$

where n_{en} is the number of nodes for a particular element, and N_A are the standard finite element shape functions. This form is useful because now $\tilde{u}$ can be written in the standard finite element form

$$\tilde{\boldsymbol{u}}^h = \sum_{A=1}^{n_{en}} N_A \boldsymbol{x}_A \tag{3.9}$$

Thus, with this choice of f^h, the component $\tilde{\boldsymbol{u}}$ of the displacement is referred to as the conforming displacement, since it conforms to the standard finite element shape functions. The vector $\hat{\boldsymbol{u}}$ is referred to as the displacement enhancement.

3.2.1 Localization condition

Given the above kinematics, it is possible to derive the conditions for localization from principles of continuum mechanics.

Consider a material undergoing standard bulk plasticity, which may follow a nonassociative flow rule. Without reviewing specific plasticity models, the model is described by a yield function $F = F(\boldsymbol{\sigma}, \boldsymbol{q})$, where $\boldsymbol{q}$ is a vector of internal state variables, a plastic potential function $G = G(\boldsymbol{\sigma}, \boldsymbol{q})$, which may be different from F, and a hardening/softening law. If $F = G$, the flow rule is associative.

To form or propagate a discontinuity on a given surface, the traction and traction rate must be continuous across that surface. The traction rate may be written

$$\begin{aligned} \dot{\boldsymbol{t}} = \boldsymbol{n} \cdot \boldsymbol{\sigma} &= \boldsymbol{n} \cdot \boldsymbol{c}^e : \dot{\boldsymbol{\epsilon}}^e && (3.10) \\ &= \boldsymbol{n} \cdot \boldsymbol{c}^e : \left(\dot{\boldsymbol{\epsilon}} - \dot{\lambda} \frac{\partial G}{\partial \boldsymbol{\sigma}} \right) && (3.11) \\ &= \boldsymbol{n} \cdot \boldsymbol{c}^e : \nabla^s \dot{\boldsymbol{u}} + \boldsymbol{n} \cdot \boldsymbol{c}^{ep} : (\llbracket \dot{\boldsymbol{u}} \rrbracket \otimes \boldsymbol{n})^s \, \delta_S && (3.12) \end{aligned}$$

where $\boldsymbol{c}^{ep}$ is the elastic-perfectly plastic modulus as shown in [51]. Hence the quantity $\boldsymbol{n} \cdot \boldsymbol{c}^{ep} : (\llbracket \dot{\boldsymbol{u}} \rrbracket \otimes \boldsymbol{n})^s$ must be zero. Exploiting the minor symmetry of $\boldsymbol{c}^{ep}$, this condition may be rewritten as

$$\boldsymbol{Q} \cdot \llbracket \dot{\boldsymbol{u}} \rrbracket = \boldsymbol{0} \tag{3.13}$$

where $\boldsymbol{Q} = \boldsymbol{n} \cdot \boldsymbol{c}^{ep} \cdot \boldsymbol{n}$ is the elastic-perfectly plastic acoustic tensor. Hence a bifurcation of the type described by the kinematics in the previous section may occur only when

$$\det \boldsymbol{Q} = 0 \tag{3.14}$$

for some normal $\boldsymbol{n}$. If we let $[\![\dot{\boldsymbol{u}}]\!] = \dot{\zeta}\boldsymbol{m}$, where $\boldsymbol{m}$ is a unit vector in the direction of the jump, then $\boldsymbol{m}$ becomes the normalized zero eigenvector for $\boldsymbol{Q}$. Hence, the localization condition returns the direction of the jump at bifurcation. This condition is similar to the weak discontinuity (strain jump) condition formulated in [11].

Localization may occur for any normal $\boldsymbol{n}$. To determine a critical normal, a numerical search algorithm in three dimensions as described in [37] and [64] is employed. A reduced version of the same algorithm has also been developed for two-dimensional problems. These algorithms are modified somewhat from the original form, as plasticity models for geomaterials often have nonassociative or kinematically hardening components. These features destroy the major symmetry of the tangent modulus assumed in the above formulations. Fortunately, the patch is relatively simple and can be accomplished simply by symmeterizing the matrix referred to as $\boldsymbol{J}$ in [37].

3.2.2 Plastic potential

In addition to the yield function, the plastic potential must also change on localization. As shown in [51], the post-localization plastic potential, Γ, exists such that plastic strain $\boldsymbol{\epsilon}^p$ evolves according to

$$\dot{\boldsymbol{\epsilon}}^p = \lambda \frac{\partial \Gamma}{\partial \boldsymbol{\sigma}} \tag{3.15}$$

This is similar bulk plasticity, but the plastic strain now takes a different form. If we assume that post-localization all plasticity occurs on the band while the bulk material unloads elastically, then the plastic consistency parameter λ can be written

$$\lambda = \lambda_\delta \delta_S \tag{3.16}$$

Regueiro and Borja [51] show that any slip on the band is rigidly plastic. Hence, the stress rate can be written

$$\dot{\boldsymbol{\sigma}} = \boldsymbol{c}^e : (\dot{\boldsymbol{\epsilon}} - \dot{\boldsymbol{\epsilon}}^p) \tag{3.17}$$

$$= \boldsymbol{c}^e : \left[\nabla^s \dot{\boldsymbol{u}} + (\llbracket \dot{\boldsymbol{u}} \rrbracket \otimes \boldsymbol{n})^s \, \delta_S - \lambda_\delta \delta_S \frac{\partial \Gamma}{\partial \boldsymbol{\sigma}} \right] \tag{3.18}$$

$$= \boldsymbol{c}^e : \nabla^s \dot{\boldsymbol{u}} + \boldsymbol{c}^e : \left[(\llbracket \dot{\boldsymbol{u}} \rrbracket \otimes \boldsymbol{n})^s - \lambda_\delta \frac{\partial \Gamma}{\partial \boldsymbol{\sigma}} \right] \delta_S \tag{3.19}$$

Since the stress rate must be bounded, this implies that

$$\lambda_\delta \frac{\partial \Gamma}{\partial \boldsymbol{\sigma}} = (\llbracket \dot{\boldsymbol{u}} \rrbracket \otimes \boldsymbol{n})^s \tag{3.20}$$

$$= \dot{\zeta} \, (\boldsymbol{m} \otimes \boldsymbol{n})^s \tag{3.21}$$

If we examine this equation more closely, we see that $\dot{\zeta} \propto \lambda_\delta$, and therefore it can be used as an alternative plastic consistency parameter for the band, with $\partial \Gamma / \partial \boldsymbol{\sigma} = (\boldsymbol{m} \otimes \boldsymbol{n})^s$. This will be convenient later, since the plastic consistency parameter now has a physical significance, and slip rate and slip distance are important parameters in many models of frictional resistance with cohesion softening. Notice that this also implies

$$\dot{\boldsymbol{\sigma}} = \boldsymbol{c}^e : \nabla^s \dot{\boldsymbol{u}} \tag{3.22}$$

In other words, the stress in the bulk material depends only on the regular part of the strain, and the slip does not affect it directly.

3.3 Background on enhanced strain element

The element used is adapted from [54] and [55]. The reader is referred to those papers for more detailed formulation of the element. The idea is that a jump in the displacement field is allowed across the element at arbitrary location, and with a slip direction $\boldsymbol{m}$, as shown in Figure 3.1. The jumps are piecewise constant across each element, and hence are not meant to capture stresses at the level of the crack tip fields. Some of the relevant details to our discussion are included below.

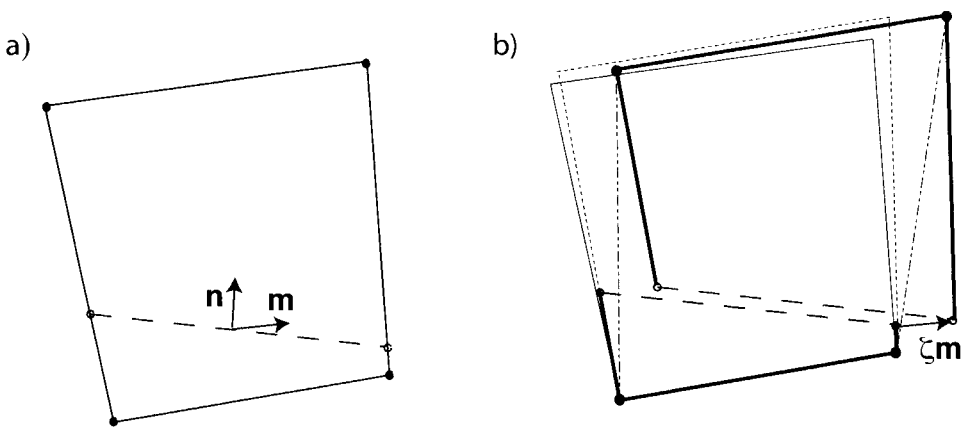

Figure 3.1: (a) Quadrilateral element showing potential slip surface. (b) Localized element with undeformed shape (fine lines), total deformed shape (bold lines), regular deformation (dotted lines), and conforming deformation (dash-dotted lines).

The Galerkin form of the equations with the enhanced strain field [54] may be written

$$\int_{\Omega^h} \nabla^s \tilde{\boldsymbol{\eta}}^h : \boldsymbol{\sigma}^h \mathrm{d}\Omega = \int_{\Omega^h} \tilde{\boldsymbol{\eta}}^h \cdot \boldsymbol{b}^h \mathrm{d}\Omega + \int_{\Gamma_t^h} \tilde{\boldsymbol{\eta}}^h : \boldsymbol{t}^h \mathrm{d}\Gamma \tag{3.23}$$

$$\int_{\Omega_{loc}^h} \hat{\boldsymbol{\gamma}} \cdot \boldsymbol{\sigma}^h \mathrm{d}\Omega = 0 \tag{3.24}$$

where Ω_{loc}^h is the domain of localized elements, $\boldsymbol{b}$ is the body force vector, and the surface traction $\boldsymbol{t}$ may be specified over some part of the boundary Γ_t^h. The weighting functions are decomposed

$$\boldsymbol{\eta}^h = \delta \boldsymbol{u}^h = \tilde{\boldsymbol{\eta}}^h + \hat{\boldsymbol{\eta}} \tag{3.25}$$

$$\nabla^s \boldsymbol{\eta}^h = \delta \boldsymbol{\epsilon}^h = \nabla^s \tilde{\boldsymbol{\eta}}^h + \nabla^s \hat{\boldsymbol{\eta}} \tag{3.26}$$

$$= \nabla^s \tilde{\boldsymbol{\eta}}^h + \hat{\gamma} \tag{3.27}$$

where $\tilde{\boldsymbol{\eta}}^h$ is the conforming part of the virtual displacement, and has the same shape functions as the conforming displacements, i.e., the standard finite element shape functions. The enhanced part of the virtual displacement, $\hat{\boldsymbol{\eta}}$, has a slightly different form from the enhanced displacement to ensure compatibility, as discussed below. To ensure stability, it is necessary for these spaces to have a null intersection [102]. Since the enhancement, as discussed below, has a delta distribution, this requirement is satisfied trivially.

The first of these equations is the standard balance of linear momentum for the quasi-static, small strain kinematics. The second equation arises from the strong discontinuity and the choice of shape functions, and allows us to determine the tractions on the discontinuity surface.

3.3.1 The stress on the band

Since the slip direction is prescribed and the amount of the slip is considered spatially constant across the element, there is a single extra degree of freedom, the slip, in each element. The slip rate is a function of the stress along the slip surface and the constitutive traction-displacement relationship along the surface. The constitutive models are discussed in later sections. It is equation (3.24), the second equation of the Galerkin form, that allows us to determine the stress on the band. In particular, we are interested the average stress along the slip surface, which we denote $\boldsymbol{\sigma}^{band}$.

We choose as our shape function for the enhancement on an element e

$$\hat{\boldsymbol{\gamma}}_e^h = \left(\delta_S - \frac{l_S^e}{a^e}\right)(\boldsymbol{\beta}^e \otimes \boldsymbol{n})^s \tag{3.28}$$

where l_S^e is the length of the shear band in the element, a^e is the element area, $\boldsymbol{\beta}^e \in R^{n_{sd}}$ is the vector of weights. This function is chosen in part because it passes the patch test for piecewise constant stress fields, i.e.

$$\int_{\Omega_{loc}^h} \hat{\boldsymbol{\gamma}} \mathrm{d}\Omega = \mathbf{0} \tag{3.29}$$

Substituting (3.28) into (3.24), we obtain

$$\int_{\Omega_e} \boldsymbol{\sigma} : \left(\delta_S - \frac{l_S^e}{a^e}\right)(\boldsymbol{\beta}^e \otimes \boldsymbol{n})^s \,\mathrm{d}\Omega \;=\; \tag{3.30}$$

$$\boldsymbol{\beta}^e \cdot \left(\int_S \boldsymbol{\sigma} \cdot \boldsymbol{n} \mathrm{d}S - \frac{l_S^e}{a^e}\int_{\Omega_e} \boldsymbol{\sigma} \cdot \boldsymbol{n} \mathrm{d}\Omega\right) \;=\; 0 \tag{3.31}$$

This implies

$$\frac{1}{a^e}\int_{\Omega_e}\boldsymbol{\sigma}\cdot\boldsymbol{n}\mathrm{d}\Omega=\frac{1}{l_S^e}\int_S\boldsymbol{\sigma}\cdot\boldsymbol{n}\mathrm{d}S=\boldsymbol{\sigma}^{band}\cdot\boldsymbol{n} \tag{3.32}$$

Hence the tractions on the band can be found by averaging those components of the stress over the element. This approximation arises from our choice of shape functions. As a mesh is refined and the element stresses approach a constant value, this approximation approaches the exact value of the stress on the element. For constant stress elements, the finite element stress is exactly recovered.

The above formulation is the small strain version of the formulation in [40]. As noted in that paper, the length of the band is never actually needed in the implementation. It is worth noting that this formulation differs slightly from [1, 54], in which

$$\hat{\gamma}_e^h=\beta^e\left(\delta_S-\frac{l_S^e}{a^e}\right)\frac{\partial\Phi}{\partial\boldsymbol{\sigma}} \tag{3.33}$$

where Φ is the yield function on the surface. This formulation is also adequate, but only ensures that the stress component in the direction of $\partial\Phi/\partial\boldsymbol{\sigma}$ is equal to the average value over the element. The vector-based formulation is slightly more general, allowing for future implementation of more complex models that may have both open and sliding degrees of freedom. The numerical implementation, however, is the same for both cases.

3.4 Determining the slip on the band

Given the element technology discussed, and a constitutive model such as the simplified model presented in Section 2.3 coupled with the friction model of Section 2.4, we now have the background to solve for the slip rate on the band as well as the evolution of the internal state variables. Since this solution occurs at the element level for a given global iteration, for this determination we can consider the displacements, and hence the conforming strains, as fixed. The displacements come back into play in determining the stiffness matrix for the global iteration, discussed in the next section.

Solving for the evolution of the band exactly is a difficult task. Much like bulk plasticity, the task of finding a closed-form solution is difficult if not impossible for many models. So instead we rely on numerical time integration. In this paper the approach is based on a generalized trapezoidal scheme. We will look at the numerical

time integration scheme in two parts: first for a general friction model, and second for the particular model of interest. We have found for the latter case that some simplifications can be made. In each case, we follow the spirit of the plasticity-like formulation in [51–55].

3.4.1 Slip on the band for a general model

Assume that at some time t_n a solution is known. We wish to solve for the condition of the band at some later time t_{n+1}. Consider a general yield condition on the band at that time

$$\Phi_{n+1} = \Phi\left(\zeta_{n+1}, \dot{\zeta}_{n+1}, \boldsymbol{\theta}_{n+1}, \dot{\boldsymbol{\theta}}_{n+1}\right) = 0 \tag{3.34}$$

where $(\cdot)_n$ represents the numerical solution of the variable $(\cdot)$ at time t_n, and $\boldsymbol{\theta}$ is a vector of internal state variables, each with its own well-defined evolution laws

$$\dot{\theta}^i = \dot{\Theta}^i\left(\zeta, \dot{\zeta}, \boldsymbol{\theta}, \dot{\boldsymbol{\theta}}\right) \tag{3.35}$$

We approach the problem using a generalized trapezoidal scheme. Given ζ_n, $\dot{\zeta}_n$, $\boldsymbol{\theta}_n$, and $\dot{\boldsymbol{\theta}}_n$, we approximate the time integration as

$$\Delta\zeta_{n+1} = \Delta t\left[\left(1-\beta_\zeta\right)\dot{\zeta}_n + \beta_\zeta\dot{\zeta}_{n+1}\right] \tag{3.36}$$

$$\theta^i_{n+1} = \theta^i_n + \Delta t\left[\left(1-\beta^i_\theta\right)\dot{\theta}^i_n + \beta^i_\theta\dot{\theta}^i_{n+1}\right] \tag{3.37}$$

β_ζ and β^i_θ are integration parameters, generally chosen between 0 and 1. If all these parameters are set to zero, the scheme is equivalent to Explicit (Forward) Euler and first-order accurate; if they are all 1 the scheme is Implicit (Backward) Euler and is first-order accurate; and if they are all 1/2 the scheme is Crank-Nicolson and is second-order accurate. For generality, we let each variable have its own time integration parameter. This strategy may be useful, for example, if one of the variables exhibited little nonlinearity and could be treated explicitly without seriously affecting

the convergence of the solution. However, for second-order accuracy, β_ζ and each β_θ^i would need to be equal to $1/2$, and all would need to be greater than $1/2$ to guarantee unconditional stability. It is expected that in most cases, all the time integration parameters would be set to the same value.

Whatever the values of the time integration parameters, we normally expect that ζ and $\boldsymbol{\theta}$ are easily written in terms of the other variables, and hence they can be eliminated from an iterative solution. To solve the system of equations, first we check for yielding, i.e. whether

$$\Phi\left(\zeta_{n+1}^{\mathrm{tr}}, 0, \boldsymbol{\theta}_{n+1}^{\mathrm{tr}}, \dot{\boldsymbol{\theta}}_{n+1}^{\mathrm{tr}}\right) > 0 \tag{3.38}$$

where $\zeta_{n+1}^{\mathrm{tr}}$ and $\boldsymbol{\theta}_{n+1}^{\mathrm{tr}}$, and $\dot{\boldsymbol{\theta}}_{n+1}^{\mathrm{tr}}$ are the values if there is no yielding at time t_{n+1}, i.e. of $\dot{\zeta}_{n+1} = 0$. Clearly, $\zeta_{n+1}^{\mathrm{tr}} = \zeta_n + (1 - \beta_\zeta)\,\dot{\zeta}_n \Delta t_{n+1}$. For a traditional plasticity-type model, where the internal state variables remain constant if there is no yielding, $\dot{\boldsymbol{\theta}}_{n+1}^{\mathrm{tr}} = 0$, and $\theta_{n+1}^{i,\mathrm{tr}} = \theta_n^i + (1 - \beta_\theta^i)\,\dot{\theta}_n^i \Delta t_{n+1}$. However, in the model discussed previously, the internal state variables do evolve even when no yielding exists.

If yielding is detected, then we must iterate to determine the final state. This can be accomplished by a standard Newton-Raphson technique. For a given set of displacements, then, we have a set of unknowns

$$\boldsymbol{X}_{n+1} = \left\{ \begin{array}{c} \dot{\boldsymbol{\theta}}_{n+1} \\ \dot{\zeta}_{n+1} \end{array} \right\} \tag{3.39}$$

and a corresponding number of equations

$$\boldsymbol{Z} = \left\{ \begin{array}{c} \dot{\boldsymbol{\Theta}}^i\left(\zeta_{n+1}, \dot{\zeta}_{n+1}, \boldsymbol{\theta}_{n+1}, \dot{\boldsymbol{\theta}}_{n+1}\right) - \dot{\boldsymbol{\theta}}_{n+1} \\ \Phi_{n+1} \end{array} \right\} = \boldsymbol{0} \tag{3.40}$$

with an initial guess

$$\boldsymbol{X}_{n+1}^0 = \left\{ \begin{array}{c} \dot{\boldsymbol{\theta}}_{n+1}^{\mathrm{tr}} \\ 0 \end{array} \right\} \tag{3.41}$$

We iterate by the standard formula

$$\boldsymbol{X}_{n+1}^{k+1} = \boldsymbol{X}_{n+1}^{k} - \left(\frac{\mathrm{D}\boldsymbol{Z}}{\mathrm{D}\boldsymbol{X}}\right)^{-1} \boldsymbol{Z}_{n+1}^{k} \tag{3.42}$$

until there is convergence to within some relative tolerance. The inverse here is symbolic. In the implementation a linear equation solver is used.

3.4.2 Slip for combined weakening and frictional model

In the case of the rate- and state- friction model of interest, we find we can use the properties of the friction model to make some simplifications, and thus reduce the computational cost of the algorithm.

The velocity on the band is unknown when checking for yielding. For zero velocity, the coefficient of friction is zero, and can go no lower (the coefficient becomes negative for negative velocities, but this is equivalent to yielding in the opposite direction). Hence, yielding occurs when

$$\Phi = (\boldsymbol{n} \otimes \boldsymbol{l})^s : \boldsymbol{\sigma} - \tau_0 \left(1 - \tfrac{\zeta_n}{\zeta^+}\right) \geq 0 \quad \texttt{if} \quad 0 \leq \zeta_n \leq \zeta^+ \tag{3.43}$$

For simplicity in this section, $\boldsymbol{\sigma}$ will refer to the stress on the band, $\boldsymbol{\sigma}^{band}$ in previous sections. The direction of $\boldsymbol{l}$ is chosen such that the shear stress $(\boldsymbol{n} \otimes \boldsymbol{l})^s : \boldsymbol{\sigma}$ is positive. Hence, once the residual cohesion disappears, the band yields automatically. Low shear stresses will result in far lower velocities, giving the appearance of minimal slip. It is a property of the friction model, however, that slip will occur under any condition with non-zero shear stress.

Once slip is detected, the magnitude of the slip must be determined. Since the integration over a time step is complicated, we will implement an approximate integration scheme of the generalized trapezoidal form. The incremental consistency condition becomes

$$0 = \Phi_{n+1} \tag{3.44}$$

$$= \left[(\boldsymbol{n} \otimes \boldsymbol{l})^s + \mu_{n+1} (\boldsymbol{n} \otimes \boldsymbol{n})\right] : \boldsymbol{\sigma}_{n+1} - c_{n+1} \tag{3.45}$$

where

$$\mu_{n+1} = A \operatorname{arcsinh}\left[\frac{\dot{\zeta}_{n+1}}{2V^*}\exp\left(\frac{\mu^* + B\ln\left(\theta_{n+1}/\theta^*\right)}{A}\right)\right] \tag{3.46}$$

$$c_{n+1} = \begin{cases} \left(1 - \zeta_{n+1}/\zeta^+\right)\left(\tau_0 - \mu_{n+1}\sigma_{n+1}\right) & \texttt{if} \quad 0 \leq \zeta_{n+1} \leq \zeta^+ \\ 0 & \texttt{if} \quad \zeta_{n+1} > \zeta^+ \end{cases} \tag{3.47}$$

$$\boldsymbol{\sigma}_{n+1} = \boldsymbol{\sigma}_n + \boldsymbol{c}^e : \left[\Delta\tilde{\boldsymbol{\epsilon}} - \Delta\zeta_{n+1}\left(\nabla f^h \otimes \boldsymbol{m}\right)^s\right] \tag{3.48}$$

After a given global iteration the displacements, and hence the conforming strains, are given. This will differ from the determination of the consistent stiffness matrix, which will be discussed later. Hence, the remaining equations become

$$\Delta\zeta_{n+1} = \Delta t\left[\left(1 - \beta_\zeta\right)\dot{\zeta}_n + \beta_\zeta\dot{\zeta}_{n+1}\right] \tag{3.49}$$

$$\dot{\theta}_{n+1} = 1 - \frac{\theta_{n+1}\dot{\zeta}_{n+1}}{D_c} \tag{3.50}$$

$$\theta_{n+1} = \theta_n + \Delta t\left[\left(1 - \beta_\theta\right)\dot{\theta}_n + \beta_\theta\dot{\theta}_{n+1}\right] \tag{3.51}$$

Here again, the time integration parameters β_ζ and β_θ may be different if one wishes to treat the time evolution of the slip and internal variable in a different manner.

For this model it is not difficult to simplify the formulation and consider only a single independent variable. In this case, it is easiest to choose the slip rate $\dot{\zeta}_{n+1}$. To start, let us combine equations (3.50) and (3.51).

$$\theta_{n+1} = \theta_n + \Delta t\left[\left(1 - \beta_\theta\right)\dot{\theta}_n + \beta_\theta\left(1 - \frac{\theta_{n+1}\dot{\zeta}_{n+1}}{D_c}\right)\right] \tag{3.52}$$

$$\left(1 + \frac{\beta_\theta\dot{\zeta}_{n+1}\Delta t}{D_c}\right)\theta_{n+1} = \theta_n + \Delta t\left[\left(1 - \beta_\theta\right)\dot{\theta}_n + \beta_\theta\right] \tag{3.53}$$

$$\left(D_c + \beta_\theta\dot{\zeta}_{n+1}\Delta t\right)\theta_{n+1} = D_c\left\{\theta_n + \Delta t\left[\left(1 - \beta_\theta\right)\dot{\theta}_n + \beta_\theta\right]\right\} \tag{3.54}$$

$$\theta_{n+1} = \frac{D_c\left\{\theta_n + \Delta t\left[\left(1 - \beta_\theta\right)\dot{\theta}_n + \beta_\theta\right]\right\}}{D_c + \beta_\theta\dot{\zeta}_{n+1}\Delta t} \tag{3.55}$$

The remaining variables in (3.45) are then functions only of $\dot{\zeta}_{n+1}$. Hence we can set up a single-variable Newton-Raphson iteration. To do this we need only derivative $\partial\Phi_{n+1}/\partial\dot{\zeta}_{n+1}$, which is given in Appendix A.

There are two differences from the traditional implicit Euler implementation for bulk plasticity that are worth noting. First, if at time t_{n+1} there is no yielding ($\dot{\zeta} = 0$), there may still be plastic slip over the step if there was yielding in the previous step and $\beta_\zeta \neq 1$. This property may be seen by examining at equation (3.49). For $\dot{\zeta} = 0$, this becomes

$$\Delta\zeta_{n+1} = \Delta t\,(1 - \beta_\zeta)\,\dot{\zeta}_n \tag{3.56}$$

The conforming strain increment used to check for yielding at t_{n+1} may then be different from the regular strain increment at that time.

The second note is that, since we have chosen the healing form of the evolution equations, the internal state variables evolve even over a fully elastic step. The equations for evolution for the state variable become

$$\dot{\theta}_{n+1} = 1 \tag{3.57}$$

$$\theta_{n+1} = \theta_n + \Delta t\left[(1 - \beta_\theta)\,\dot{\theta}_n + \beta_\theta\right] \tag{3.58}$$

Notice that the state variable evolves even if there is no yielding over several steps. This formulation could cause numerical problems were it not for the fact the actual yield condition (3.43) is independent of θ. If this were not the case, one may have to verify convexity over stress space $\times$ loading space, which would likely be nontrivial.

We have now reduced the problem to a single-variable Newton-Raphson iteration. A summary of the algorithm appears in the Box 3.1.

3.5 Consistent stiffness matrix

To solve the global finite element problem, we must form a stiffness matrix for this element. Since we have performed a numerical time integration scheme, this tangent stiffness should be consistent with the time stepping for quadratic convergence. This consistency is analogous to the consistent or algorithmic tangent modulus for continuum algorithms.

Similarly to [55], we will see that the slip rate and internal state variables can be eliminated at the element level by modifying the element stiffness matrix. Hence the

Box 3.1 Summary of incremental jump algorithm

Step 1. Compute $\boldsymbol{\sigma}^{\mathrm{tr}}_{n+1} = \boldsymbol{\sigma}_n + \boldsymbol{c}^e : \Delta\boldsymbol{\epsilon}^{conf}$

Step 2. Check yielding: is $\boldsymbol{\sigma}^{tr} : (\boldsymbol{n} \otimes \boldsymbol{l}) > \tau_0 \left(1 - \zeta_n/\zeta^+\right)$?

If no, band is inactive. Set

$\boldsymbol{\sigma}_{n+1} = \boldsymbol{\sigma}^{\mathrm{tr}}_{n+1}$,

$\dot{\zeta}_{n+1} = 0$,

$\Delta\zeta_{n+1} = \Delta t \left(1 - \beta_\zeta\right) \dot{\zeta}_n$,

$\dot{\theta}_{n+1} = 1$,

$\theta_{n+1} = \theta_n + \Delta t \left[\left(1 - \beta_\theta\right) \dot{\theta}_n + \beta_\theta\right]$,

and exit.

Step 3. Set $\dot{\zeta}^0_{n+1} = V^*$,

Step 4. Iterate

$$\Delta\zeta^k_{n+1} = \Delta t \left[\left(1 - \beta_\zeta\right) \dot{\zeta}^k_n + \beta_\zeta \dot{\zeta}_{n+1}\right]$$

$$\theta^k_{n+1} = D_c \left\{\theta_n + \Delta t \left[\left(1 - \beta_\theta\right) \dot{\theta}_n + \beta_\theta\right]\right\} / \left(D_c + \beta_\theta \dot{\zeta}^k_{n+1} \Delta t\right)$$

$$\dot{\zeta}^{k+1}_{n+1} = \dot{\zeta}^k_{n+1} - \Phi\left(\dot{\zeta}^k_{n+1}, \Delta\zeta^k_{n+1}, \theta^k_{n+1}\right) / \left[\partial\Phi\left(\dot{\zeta}^k_{n+1}, \Delta\zeta^k_{n+1}, \theta^k_{n+1}\right) / \partial\dot{\zeta}\right]$$

until $|\Phi^k_{n+1}| / |\Phi^0_{n+1}| < \mathrm{tol}$

Step 5. Store $\dot{\zeta}_{n+1}$, $\Delta\zeta_{n+1}$, θ_{n+1} and $\dot{\theta}_{n+1} = 1 - \theta_{n+1}\dot{\zeta}_{n+1}/D_c$ exit.

other element-level variables need not be added to the global solution routine, and the finite element program can solve for the displacements without modification.

3.5.1 Stiffness matrix for a general model

Following the implementation of a general friction model in the previous section, we discuss here how to modify the stiffness matrix for the case of yielding. The governing equations are similar, but we now consider that the element nodes may also move, so we add the balance of linear momentum for the small strain quasi-static loading. The equations become:

$$\boldsymbol{r}^e = \int_{\Omega^e} \boldsymbol{B}^t : \boldsymbol{\sigma} \mathrm{d}\Omega - \int_{\Omega^e} \boldsymbol{N}^t \boldsymbol{b} \mathrm{d}\Omega - \int_{\Gamma^e} \boldsymbol{N}^t \boldsymbol{t} \mathrm{d}\Gamma = \boldsymbol{0} \tag{3.59}$$

$$\boldsymbol{\vartheta} = \dot{\boldsymbol{\Theta}}^i \left(\zeta_{n+1}, \dot{\zeta}_{n+1}, \boldsymbol{\theta}_{n+1}, \dot{\boldsymbol{\theta}}_{n+1}\right) - \dot{\boldsymbol{\theta}}_{n+1} = \boldsymbol{0} \tag{3.60}$$

$$\Phi_{n+1} = 0 \tag{3.61}$$

where $\boldsymbol{N}$ is the standard matrix of finite element shape functions, and we consider $\boldsymbol{B}$ here as the third-order strain-dispalcement tensor, i.e. $B_{ijk} d_k = \epsilon_{ij}$. In the implement, the corresponding matrix forms are used for computational efficiency.

Taking variations of these quantities, we arrive at

$$\delta \boldsymbol{r}^e = \boldsymbol{K}^e_{dd}\delta \boldsymbol{d}^e + \boldsymbol{K}^e_{d\dot{\theta}}\delta\dot{\boldsymbol{\theta}} + \boldsymbol{K}^e_{d\dot{\zeta}}\delta\dot{\zeta} \tag{3.62}$$

$$\delta \boldsymbol{\vartheta} = \boldsymbol{K}^e_{\dot{\theta}d}\delta \boldsymbol{d}^e + \boldsymbol{K}^e_{\dot{\theta}\dot{\theta}}\delta\dot{\boldsymbol{\theta}} + \boldsymbol{K}^e_{\dot{\theta}\dot{\zeta}}\delta\dot{\zeta} \tag{3.63}$$

$$\delta \Phi = \boldsymbol{K}^e_{\dot{\zeta}d}\delta \boldsymbol{d}^e + \boldsymbol{K}^e_{\dot{\zeta}\dot{\theta}}\delta\dot{\boldsymbol{\theta}} + K^e_{\dot{\zeta}\dot{\zeta}}\delta\dot{\zeta} \tag{3.64}$$

The first quantity, $\boldsymbol{K}^e_{dd}$, is the standard element stiffness matrix. The four parts of the stiffness comprising the lower righthand portion,

$$\boldsymbol{K}^e_{\dot{\theta}\dot{\theta}} = \frac{\partial \boldsymbol{\vartheta}}{\partial \dot{\boldsymbol{\theta}}} \tag{3.65}$$

$$\boldsymbol{K}^e_{\dot{\theta}\dot{\zeta}} = \frac{\partial \boldsymbol{\vartheta}}{\partial \dot{\zeta}} \tag{3.66}$$

$$\boldsymbol{K}^e_{\dot{\zeta}\dot{\theta}} = \frac{\partial \Phi}{\partial \dot{\boldsymbol{\theta}}} \tag{3.67}$$

$$K^e_{\dot{\zeta}\dot{\zeta}} = \frac{\partial \Phi}{\partial \dot{\zeta}} \tag{3.68}$$

are the same quantities used to determine the slip on the band, and the same code can be reused. The final four quantities are

$$\boldsymbol{K}^e_{d\dot{\theta}} = \frac{\partial \boldsymbol{r}^e}{\partial \dot{\boldsymbol{\theta}}} \tag{3.69}$$

$$\boldsymbol{K}^e_{d\dot{\zeta}} = \frac{\partial \boldsymbol{r}^e}{\partial \dot{\zeta}} = -\int_{\Omega^e} \boldsymbol{B}^t : \boldsymbol{c}^e : \left(\nabla f^h_e \otimes \boldsymbol{m}\right)^s \mathrm{d}\Omega \beta_\zeta \Delta t \tag{3.70}$$

$$\boldsymbol{K}^e_{\dot{\theta}d} = \frac{\partial \boldsymbol{\vartheta}}{\partial \boldsymbol{d}^e} \tag{3.71}$$

$$\boldsymbol{K}^e_{\dot{\zeta}d} = \frac{\partial \Phi}{\partial \dot{\zeta}} \tag{3.72}$$

Most of the quantities above depend on the constitutive response, and cannot be specified further in this section. In some cases, we can provide more information. For example, if the state variables are only affected by the nodal displacements through the stress, then

$$\boldsymbol{K}^e_{\dot{\theta}d} = \frac{\partial \dot{\boldsymbol{\theta}}}{\partial \boldsymbol{\sigma}} : \frac{\partial \boldsymbol{\sigma}}{\partial \boldsymbol{d}^e} = \frac{1}{a^e} \int_{\Omega^e} \frac{\partial \dot{\boldsymbol{\theta}}}{\partial \boldsymbol{\sigma}} : \boldsymbol{c}^e : \boldsymbol{B}^e \mathrm{d}\Omega \tag{3.73}$$

Finally, we note that, since the state variables and the slip rate are element quantities that do not affect surrounding elements, we can statically condense the stiffness matrix, following Borja and Regueiro [55].

$$\boldsymbol{K}^e = \boldsymbol{K}^e_{dd} - \begin{bmatrix} \boldsymbol{K}^e_{d\dot{\theta}} & \boldsymbol{K}^e_{d\dot{\zeta}} \end{bmatrix} \begin{bmatrix} \boldsymbol{K}^e_{\dot{\theta}\dot{\theta}} & \boldsymbol{K}^e_{\dot{\theta}\dot{\zeta}} \\ \boldsymbol{K}^e_{\dot{\zeta}\dot{\theta}} & K^e_{\dot{\zeta}\dot{\zeta}} \end{bmatrix}^{-1} \begin{bmatrix} \boldsymbol{K}^e_{\dot{\theta}d} \\ \boldsymbol{K}^e_{\dot{\zeta}d} \end{bmatrix} \tag{3.74}$$

The great advantage of this strategy is that all variables except the nodal displacements are condensed out at the element level, so the global solution algorithm can simply input the element stiffness matrix (3.74) with no modification.

3.5.2 Stiffness matrix for combined weakening and frictional model

Once the jump increment and internal state variable θ have been solved for for a given set of displacements, the tangent stiffness matrix consistent with this algorithm falls out with relatively little modification if we follow [55]. Two conditions must be met

$$\boldsymbol{r}^e = \int_{\Omega^e} \boldsymbol{B}^t : \boldsymbol{\sigma} \mathrm{d}\Omega - \int_{\Omega^e} \boldsymbol{N}^t \boldsymbol{b} \mathrm{d}\Omega - \int_{\Gamma^e} \boldsymbol{N}^t \boldsymbol{t} \mathrm{d}\Gamma = 0 \tag{3.75}$$

$$\Phi_{n+1} = 0 \tag{3.76}$$

Since we now have only the variables $\boldsymbol{d}$ and $\dot{\zeta}$ as independent, taking a variation on these equations results in

$$\delta \boldsymbol{r}^e = \boldsymbol{K}^e_{dd} \delta \boldsymbol{d}^e + \boldsymbol{K}^e_{d\dot{\zeta}} \delta \dot{\zeta}^e \tag{3.77}$$

$$\delta \Phi = \boldsymbol{K}^e_{\dot{\zeta}d} \delta \boldsymbol{d}^e + \boldsymbol{K}^e_{\dot{\zeta}\dot{\zeta}} \delta \dot{\zeta}^e \tag{3.78}$$

where

$$\boldsymbol{K}^e_{dd} = \int_{\Omega^e} \boldsymbol{B}^t : \boldsymbol{c}^e : \boldsymbol{B} \mathrm{d}\Omega \tag{3.79}$$

$$\boldsymbol{K}^e_{d\dot{\zeta}} = -\int_{\Omega^e} \boldsymbol{B}^t : \boldsymbol{c}^e : \left(\nabla f_e^h \otimes \boldsymbol{m}\right)^s \mathrm{d}\Omega \beta_\zeta \Delta t \tag{3.80}$$

$$\boldsymbol{K}^e_{\dot{\zeta}d} = \frac{\partial \Phi}{\partial \boldsymbol{d}} \tag{3.81}$$

$$\boldsymbol{K}^e_{\dot{\zeta}\dot{\zeta}} = \frac{\partial \Phi}{\partial \dot{\zeta}} \tag{3.82}$$

The last quantity we already have. The third quantity is:

$$\frac{\partial \Phi}{\partial \boldsymbol{d}} = \frac{1}{a^e} \int_{\Omega^e} \frac{\partial \Phi}{\partial \boldsymbol{\sigma}} : \boldsymbol{c}^e : \boldsymbol{B} \mathrm{d}\Omega \tag{3.83}$$

$$= \begin{cases} (a^e)^{-1} \int_{\Omega^e} \left[(\boldsymbol{n} \otimes \boldsymbol{l})^s + \frac{\zeta}{\zeta^+} \mu (\boldsymbol{n} \otimes \boldsymbol{n}) \right] : \boldsymbol{c}^e : \boldsymbol{B} \mathrm{d}\Omega & \texttt{if} \quad \zeta \leq \zeta^+ \\ (a^e)^{-1} \int_{\Omega^e} \left[(\boldsymbol{n} \otimes \boldsymbol{l})^s + \mu (\boldsymbol{n} \otimes \boldsymbol{n}) \right] : \boldsymbol{c}^e : \boldsymbol{B} \mathrm{d}\Omega & \texttt{if} \quad \zeta > \zeta^+ \end{cases} \tag{3.84}$$

where the subscripts $n+1$ have been omitted for convenience. As before, the slip rate can be statically condensed out, and the resulting element stiffness matrix is

$$\boldsymbol{K}^e = \boldsymbol{K}^e_{dd} - \boldsymbol{K}^e_{d\dot{\zeta}} K^{e\,-1}_{\dot{\zeta}\dot{\zeta}} \boldsymbol{K}^e_{\dot{\zeta}d} \tag{3.85}$$

3.6 Band tracking algorithm

The band tracking strategy employed is of the type that Oliver and coworkers have termed a local strategy. This method is in contrast to a global strategy described in [48, 49] , or level-set methods employed in [62]. The idea is to track the band as it propagates from element to element, explicitly keeping track of the coordinates where the band intersects an element edge.

Prior to the onset of localization, the bifurcation condition is checked at the end of each time step. Once localization is detected in at least one element, the band tracking

begins. First, a root element must be determined. Usually, we choose the element that has the least value of det $\boldsymbol{Q}$ as the first root element. However, for special cases such as homogeneous deformation, we choose a root element or elements. For homogeneous deformation, all the elements bifurcate at the same time. In reality though, some perturbation will trigger earlier localization in some location or locations, which for the sake of those problems we specify.

Once a root element is detected, that element is traced through the centroid using the critical normal, and the endpoints of the band are calculated and recorded. To determine the points of intersection, we note that the edges intersected by the discontinuity are those with an active node at one end and an inactive node at the other. Since the active nodes are already needed to determine the function f^h, it is computationally trivial to loop over the edges to find the edges of intersection. Assuming the element edges are straight, the intersection point $\boldsymbol{x}$ can be determined from the system of equations

$$\boldsymbol{x} = \boldsymbol{x}_s^e + \alpha \boldsymbol{l} \tag{3.86}$$

$$\boldsymbol{x} = \beta \left(\boldsymbol{x}_a^e - \boldsymbol{x}_b^e \right) \tag{3.87}$$

where $\boldsymbol{x}_a^e$ and $\boldsymbol{x}_b^e$ are the coordinates end nodes of that edge, $\boldsymbol{x}_s^e$ are the coordinates of a point on discontinuity surface, and α and β are initially undetermined scalars. the vector $\boldsymbol{x}_s^e$ is taken to be the centroid of the element for a root element, otherwise it is the point of intersection of the edge and failure surface from the adjacent element. By substituting the value of $\boldsymbol{x}$ from (3.87) into (3.86), and then solving that system of two equations for α, we get

$$\alpha = \frac{|| \left(\boldsymbol{x}_a^e - \boldsymbol{x}_b^e \right) \times \left(\boldsymbol{x}_s^e - \boldsymbol{x}_a^e \right) ||}{|| \boldsymbol{l} \times \left(\boldsymbol{x}_a^e - \boldsymbol{x}_b^e \right) ||} \tag{3.88}$$

Once α is determined, we can use equation (3.86) to solve for the point of intersection.

The next elements we check are those that are adjacent to the root element at the end of the band. If these elements have localized, we want to ensure that the band is continuous across element boundaries. To find these elements, we construct an element neighbors (EN) array from the standard IEN array [103]. This array is constructed such that EN(i, j) is the number of the element adjacent to element i at local face j. If there is no neighbor there, i.e., that face is at the boundary of the body, then -1 is returned.

We use active and passive nodes of the element to locate the local edge that contains the band. Looping over the edges of an element i, if we find an edge j between an active and a passive node, then we check that

1) the EN array does not return -1

2) the element number is not already in the array, and

3) the element is not already traced.

If all these criteria are satisfied, we add the element number EN(i, j) to a variable length edge-of-band-elements array along with the coordinates of the end of the band.

We then go to the first element in the edge-of-band-elements array and check for localization. If localization is detected we trace that element, find the new neighbor, and add it to the end of the array. We then proceed to the next element, and so forth until we reach the end of the array, which may be growing throughout the tracking process.

If we are fairly certain that one band will form, we can stop there, and at subsequent time steps only check the elements in the edge-of-band-elements array. If we allow for the possibility of multiple bands, however, we now check the remaining elements for localization. If other elements have localized, we determine a new root element, and propagate a new band in the same way. We can use a single edge-of-band-elements array for this process.

At subsequent time steps, it is important to check for elements in the edge-of-band-elements array before proceeding to check for new root elements. This ensures that newly localized elements are added to existing bands. The algorithm is summarized in Box 3.2.

3.7 Numerical examples

3.7.1 Sliding of a pre-fractured block

The first example consists of a 1-meter $\times$ 1-meter block, discretized into 9 elements, and with a strong discontinuity inserted horizontally through the center. The exaggerated conforming deformations are shown in Figure 3.2. The mesh was then refined to 81 elements. As the sample is pre-fractured, the initial shear stress is zero. The ability to pre-fracture a sample was added to the code to test the convergence of the friction algorithm and to verify the properties of the friction model.

The material properties are listed in Table 3.1. These properties are taken to simulate a granite, with most of the frictional properties taken from [21], except for μ^* and

Box 3.2. Summary of band tracking algorithm, performed at the end of each time step

Step 1. If localization has not begun, check for localization, of all elements. If localization is detected, choose element with the least value of $\det \boldsymbol{Q}$, and perform *localize* subroutine. If not, exit.

Step 2. Move to first element of edge-of-band-elements array. If the array is empty, exit. Otherwise, go to step 3.

Step 3. Check for localization of element in array. If localization detected, perform *localize* subroutine and delete from array.

Step 4. Move to next element in array. If at the end, exit. Otherwise, go to step 3.

Step 5. If allowing for multiple bands: Check for remaining, untraced elements that may have localized. If localization is detected, choose element with least value of $\det \boldsymbol{Q}$, and perform *localize* subroutine and go to step 3. If not, exit.

localize subroutine
Step 1. Trace element according to normal and coordinate (either from information in edge-of-band-elements array or centroid)

Step 2. Go to first element edge.

Step 3. If current edge has one active and one inactive end node *and* neighbor element exists *and* that element has not yet been traced *and* that element is not already in the edge-of-band elements array, determine coordinates of intersection of band and element edge, and add to edge-of-band-elements array.

Step 4. If all edges have been check or both ends of band have been found, exit. Otherwise, go to step 3.

the elastic properties, which are taken from typical values for granite.

As Figure 3.3 shows, the finite element model captures the variation in the coefficient of friction exhibited by the friction model. As motion starts, the friction coefficient rapidly rises and dips to steady state. We might expect a faster rise in the friction coefficient, but there is little shear stress to drive this rise initially. As the slip speed is increased, the characteristic spike and drop to a lower steady-state value is seen. Similarly, when the velocity is dropped again, the coefficient of friction dips and then rises to a new, higher value. The elastic parameters are quite stiff compared to the frictional parameters, and hence the elasticity plays little role in the material behavior. The refinement shows results that are quite comparable to the initial run. The response is initially slightly stiffer, but shows less of a peak in the initial rise. Once the friction reaches steady state for the first time, the solutions are nearly identical.

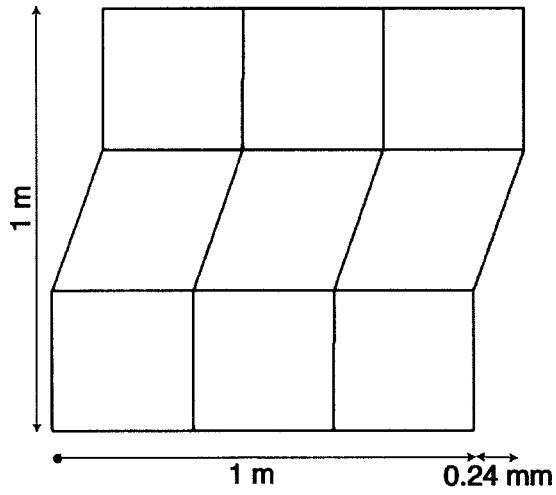

Figure 3.2: Deformed shape for example 1 showing conforming displacements, multiplied 100 times. The failure surface passes horizontally through the center of the three center elements. Since the global finite element needs no information about the band, the postprocessor uses standard nodal interpolations.

Table 3.2 shows the convergence rate for the various methods, using the coefficient of friction as the parameter of interest. We use a time of 4.2 seconds, when the friction coefficient is still changing, as our gauge. At the end of the run, the solution is too close to steady state and the convergence rates tend to look better than the methods would predict. Explicit Euler, Crank-Nicolson, and Implicit Euler runs were each made with time steps of 0.2, 0.02, and 0.002 seconds. The "exact" solution was then obtained by running a Crank-Nicolson simulation with a time step of 0.0002 seconds.

Table 3.1: Material properties for granite direct shear test.

Parameter	symbol	value
Young's Modulus	E	5500 MPa
Poisson's Ratio	ν	0.25
Reference Friction Coefficient	μ^*	0.72
Velocity Variation Coefficient	A	0.0012
State Variable Variation Coefficient	B	0.00135
Velocity Normalizing Constant	V^*	1.0 μm/s
State Variable Normalizing Constant	θ^*	2.25
Characteristic Sliding Distance	D_c	μm

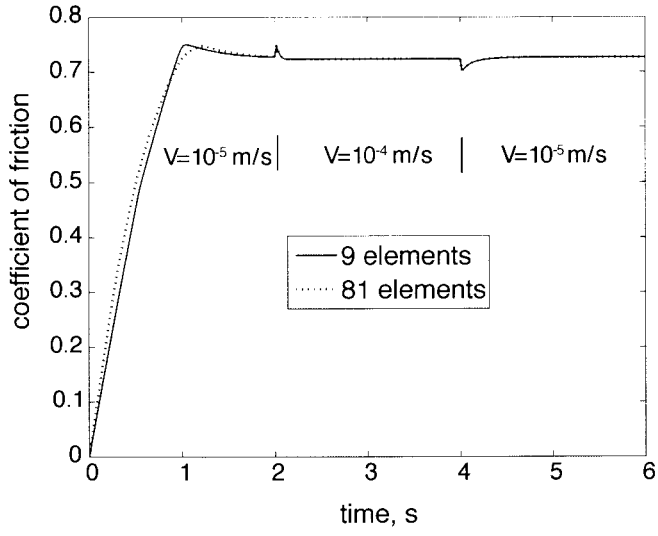

Figure 3.3: Coefficient of friction as a function of time under the prescribed displacements for direct shear example.

Not surprisingly, the explicit simulation diverged for large time steps. Only the last run converged, leaving no comparisons to check the convergence rate. However, the error is of the same order as the Implicit Euler run for that time step, which suggests that the method is behaving as expected. Implicit Euler shows the expected first-order convergence, while the Crank-Nicolson scheme shows convergence slightly faster than second-order rate would predict. The Crank-Nicolson simulation with a time step of 0.2 seconds failed to converge in a Newton iteration, which is not related to the stability of the problem. This problem could have been solved by step cutting, but this process would affect the error. The results are shown in Table 3.2

3.7.2 Plane strain compression of a laboratory sample

The second example is a plane strain compression simulation of San Marcos gabbro. This test is meant to recreate a two-dimensional version of the triaxial test G3 described in Wong [80] in the slip weakening stage. The simulation was initially reported

Table 3.2: Error as a function of the number of time steps at 4.2 seconds. Error calculated using an "exact" solution of 30000 time steps with the Crank-Nicolson scheme. Entries with a * did not converge.

Number of time steps	Explicit Euler	Crank-Nicolson	Implicit Euler
30	*	*	3.0431E − 03
300	*	1.1540E − 03	6.6593E − 04
3000	7.8128E − 05	1.1749E − 06	7.1984E − 05

in [97]. The material parameters are shown in Table 3.3. The elastic parameters are taken from typical values for gabbro. The plasticity model is a Drucker-Prager model with linear hardening (here, softening). The parameters are set to reproduce, to the best of the information given, the forces measured in the experiment. The reference friction coefficient μ^* is taken to satisfy the recorded strength and failure geometry from the experiments. The remaining friction parameters are from a granite sample discussed in [21]. A confining pressure of 250 MPa is applied to the sides, and then the sample is compressed vertically.

Table 3.3: Material properties for plane strain compression of San Marcos gabbro.

Parameter	symbol	value
Young's Modulus	E	5500 MPa
Poisson's Ratio	ν	0.25
Cohesive Strength Parameter	α	8.034 MPa
Friction Parameter	β	0.633
Dilatation Parameter	b	0.633
Hardening Modulus	H	-10 MPa
Reference Friction	μ^*	0.72
Velocity Variation Coefficient	A	0.0012
State Variable Variation Coefficient	B	0.00135
Velocity Normalizing Constant	V^*	1.0 μm/s
State Variable Normalizing Constant	θ^*	2.25
Characteristic Sliding Distance	D_c	μm/s

The results are shown in Figures 3.4 and 3.5. The specimen at first behaves elastically, then plastically until bifurcation is detected. Since the deformation is homogeneous, a seed element is chosen in the middle and a single band propagates from that element. For these material properties, the failure surface forms at sixty degrees from the horizontal, but could form either direction. The choice of band direction is made by an algorithm as described in [52], but in this case both choices are equally likely. In a physical specimen the direction of propagation would be chosen by flaws or slight variations in the material properties. Since we do not have information at that level for our simulation and the direction is not important for our study, we let the algorithm choose the normal based on machine roundoff error.

Once the surfaces are inserted, the sample unloads under slip weakening. The experimental information concludes noting only a final friction coefficient. However, to demonstrate the properties of the friction model at post-weakening, we add a velocity jump to the simulation. Initially, the vertical compression rate is 0.866 μm/s, which at steady state slipping would give a slip velocity of 1 μm/s on the band. However, some unstable slip occurs at first that otherwise would not be predicted by rigid block

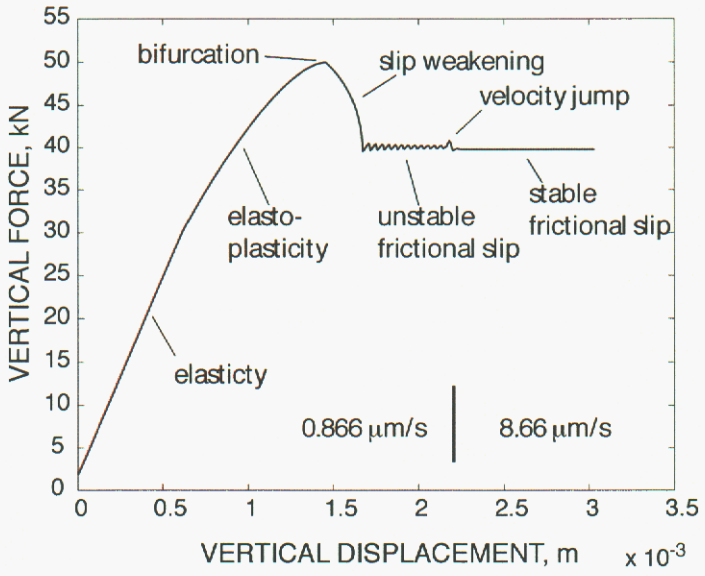

Figure 3.4: Force-displacement curve for plane strain compression showing behavior in different stages of deformation.

models. This slip is a function of the stiffness of the sample and the friction parameters, and is analogous to the spring-slider examples discussed in [20]. A velocity step is added at 2 mm total vertical displacement, resulting in the jump and dip of the friction coefficient. At the higher speed that is ten times the initial rate, slip rapidly becomes stable, as predicted by the model.

This problem was run with 1, 15, and 128 elements. Since the problem is homoge-

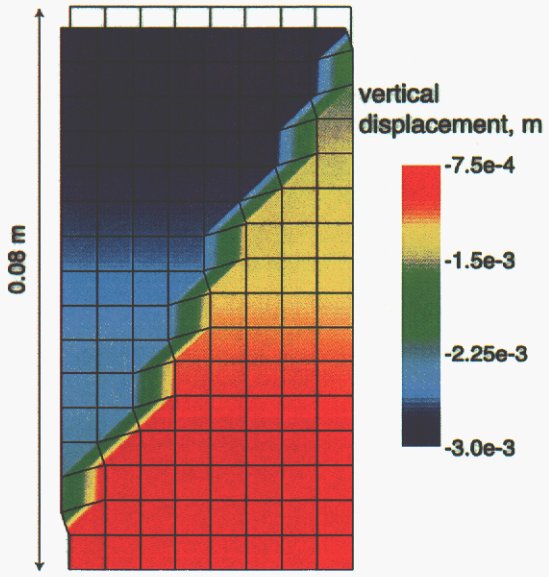

Figure 3.5: Deformed shape at the end of simulation for plane strain compression example. Black outline in background shows initial configuration.

neous, it is not surprising that the solutions are nearly identical. The relative error in the vertical force between the 15- and 128-element solutions is shown in Figure 3.6. The error in the localized phase is similar to that in the plastic phase. This error is due to the convergence tolerance in the local and element-level solutions, and the solution of the global system of equations.

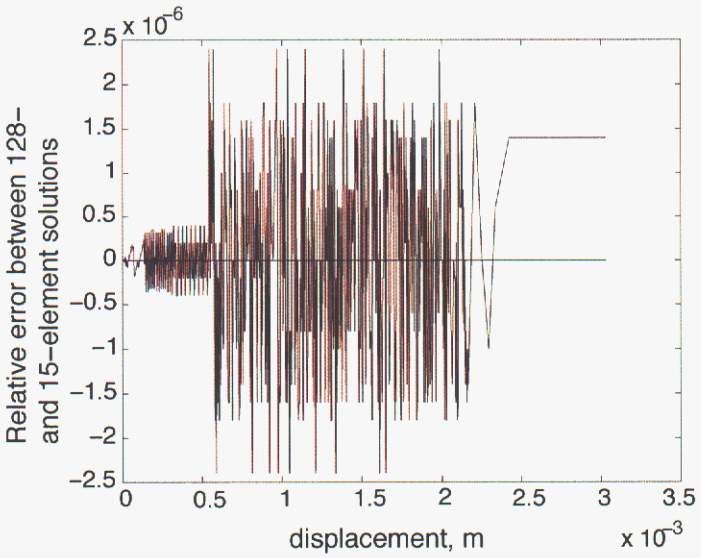

Figure 3.6: Relative error in force between 15- and 128-element solution as a function of time. The error is a result of the tolerance in the iterations, and the solution of the global equations. The error in the plastic and localized phases is comparable.

3.7.3 Shearing of sample with a hole

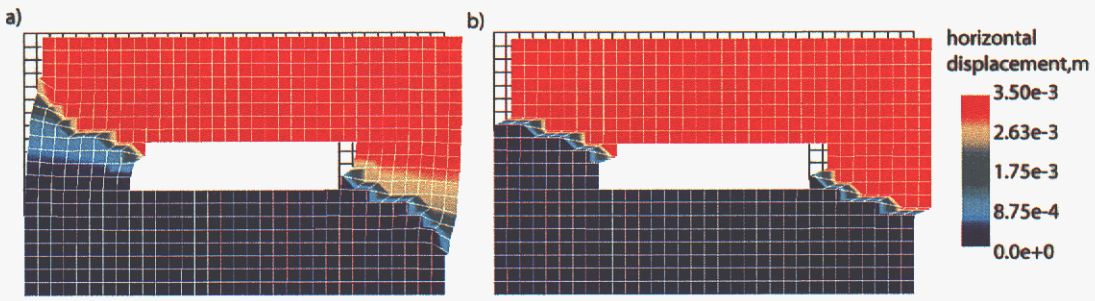

Figure 3.7: Deformed shape of the shear example with a hole, 576-element case. a) when the band is allowed to propagate in the critical direction, locking effects lead to additional bulk plasticity and new bands. Notice the increased bulk dilatation over b) where the sample unloads elastically after the straight band propagates. Undeformed shape shown in background in black outline.

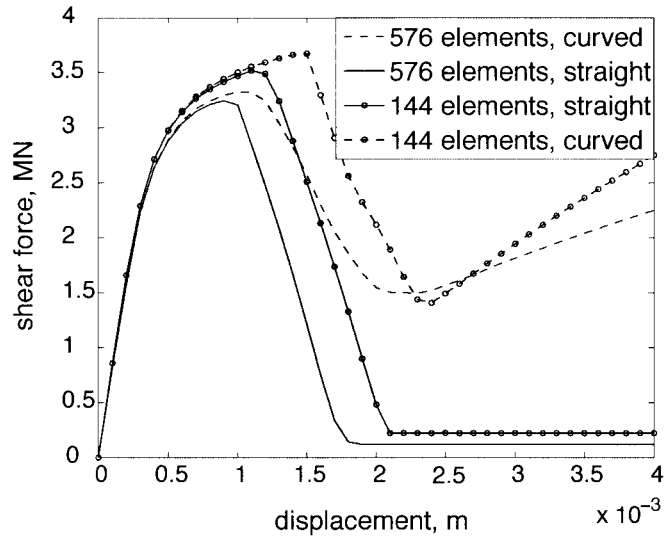

Figure 3.8: Force-displacement curve for shearing of example with hole in it. If the band is forced to propagate in a straight line, the resistance drops to a purely frictional response. If the band is allowed to propagate in the critical direction, it initially softens, but locking effects due to the changing direction eventually create hardening.

As we move to more complex problems, some interesting issues arise. We start by simulating the shearing of an 80- $\times$ 100-cm block with a hole in it as shown in Figure 3.7 to test the tracking of multiple bands. In this case the friction coefficient is constant, and material properties are listed in Table 3.4.

Table 3.4: Material properties for shear example with hole.

Parameter	symbol	value
Young's Modulus	E	9000 MPa
Poisson's Ratio	ν	0.15
Cohesive Strength Parameter	α	8.034 MPa
Friction Parameter	β	0.633
Dilatation Parameter	b	0.3165
Hardening Modulus	H	0 MPa
Friction Coefficient	μ	0.6

The initial results show that the band propagates through the sample and initially there is significant softening (see Figure 3.8), but this is followed by hardening. This hardening is due to a locking effect as surfaces in adjacent elements attempt to slip in different directions. To some extent, this reflects a physical process in that changing directions on surfaces do create an increased resistance to slip. Elements with opening

and perhaps rotational degrees of freedom to the surface, such as [48, 66], could change the kinematics of slip, allowing for local areas of opening. For comparison, we also rerun the problem but force the band to propagate in a straight line. In this case the sample softens to a purely frictional response, and little bulk plasticity is seen in the rest of the sample. The original simulation shows significant bulk plasticity, including dilatation, and even creates newly localized bands (these new bands do not slip very much and hence are not visible in the deformed shape).

The problem is run with 144 and 576 elements. The response is slightly softer for the 576-element case, but similar. The refined mesh naturally detects plasticity and localization earlier, as there are more points to sample. In the straight band case, the initial angle of the band is slightly more vertical, resulting in a lower frictional response. In the curved band case, the refinement shows slightly less softening before the stress locking occurs, but the residual slope is lower.

3.7.4 Compression of sample with a hole

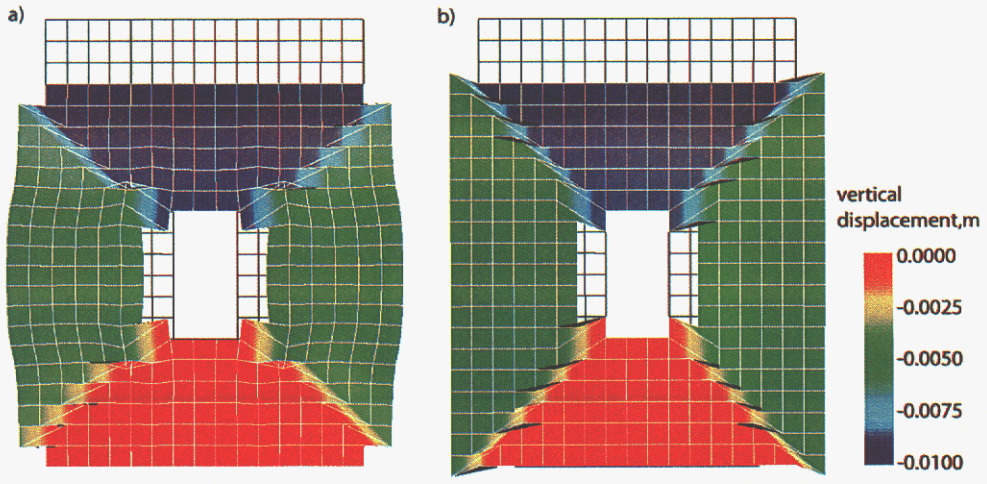

Figure 3.9: Deformed shape for compression of sample with hole in it, 336-element case. a) Bulk deformation increases after the curving band locks up, while b) the straight band allows for elastic unloading of the bulk sample. Undeformed shape shown in background in black outline.

We also run a compression test of a 50- $\times$ 70-cm sample with a hole in it, shown in Figure 3.9. The frictional variation is the same as the San Marcos gabbro sample. When compressed, bands propagate from the interior corners of the sample. Similarly to the shear example, if the band is allowed to change direction in different elements, there is a locking effect after some initial softening. The locking results again in significant bulk deformation and plasticity later on in the deformation process. Again, if the bands are forced to propagate in a straight line, the sample unloads elastically after bifurcation. A comparison of the force-displacement responses is shown in Figure 3.10.

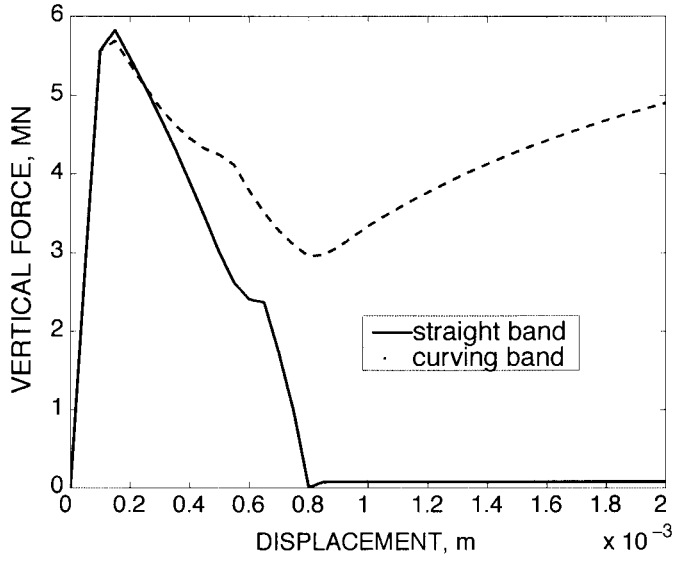

Figure 3.10: Force-displacement curve for compression of example with hole in it, 336-element case. If the band is forced to propagate in a straight line, the resistance drops to a purely frictional response. If the band is allowed to propagate in the critical direction, it initially softens, but locking effects due to the changing direction eventually create hardening.

Mesh refinements show similar responses. The problem was run with 48-, 336-, and 2734-element meshes. For the straight band case (Figure 3.11) the only significant difference between the 336- and 2734-element meshes is that band seems to stop propagating for a couple steps in the 336-element case. This behavior disappears upon refinement. In the curved band case (Figure 3.12) locking shows up sooner, as may be expected when the elements are smaller, but the residual slope of the force-displacement curve is less.

3.7.5 Plane strain example with GeoModel

Finally, we combine the enhanced strain element with the GeoModel described in [2]. The problem is a plane strain compression problem with the same geometry and frictional properties as the first plane strain example. The bulk material properties are taken from the limestone properties reported in that paper.

The resulting force-displacement curve is shown in Figure 3.13, with a close-up of the oscillations shown in Figure 3.14. Since the elastic properties are stiffer, there is less oscillation. The other significant difference is that there is more bulk plasticity before localization. Since the model as implemented is associative and has no softening, there is no localization until perfect plasticity is reached. An implementation of the non-associative formulation may predict earlier localization.

The deformed shape is shown in Figure 3.15. The critical angle, although still greater

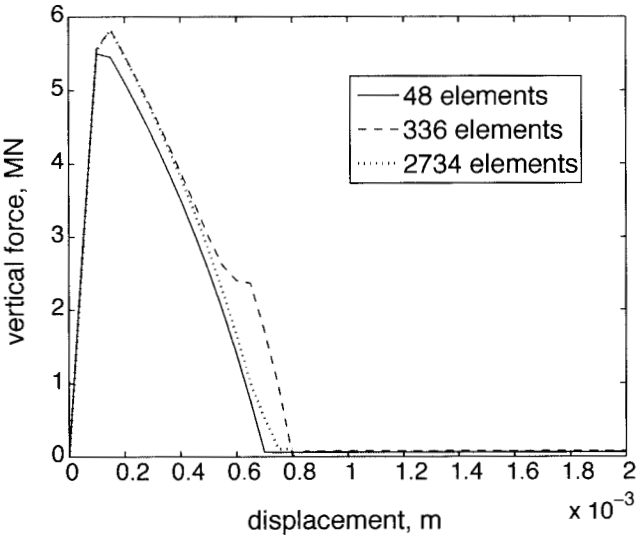

Figure 3.11: Results of mesh refinement for compression example with a hole in it for straight band. The results appear to converge. The only significant difference between the 336- and 2734-element solutions is one point in the 336-element solution where the band stops propagating momentarily.

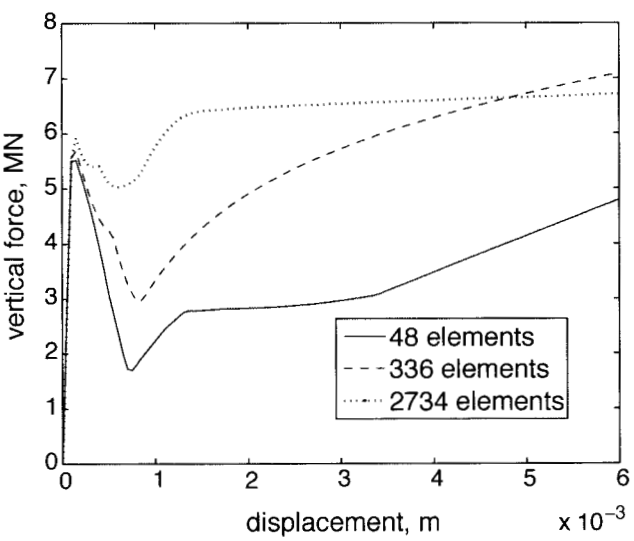

Figure 3.12: Results of mesh refinement for compression example with a hole in it for curving band. As the mesh is refined, locking occurs earlier, but the residual slope of the force-displacement curve decreases.

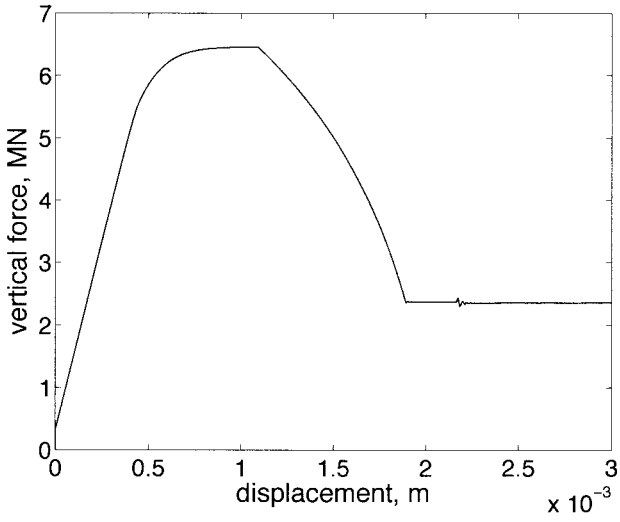

Figure 3.13: Force-displacement curve for GeoModel, showing elasticity, bulk plasticity, slip weakening and friction response.

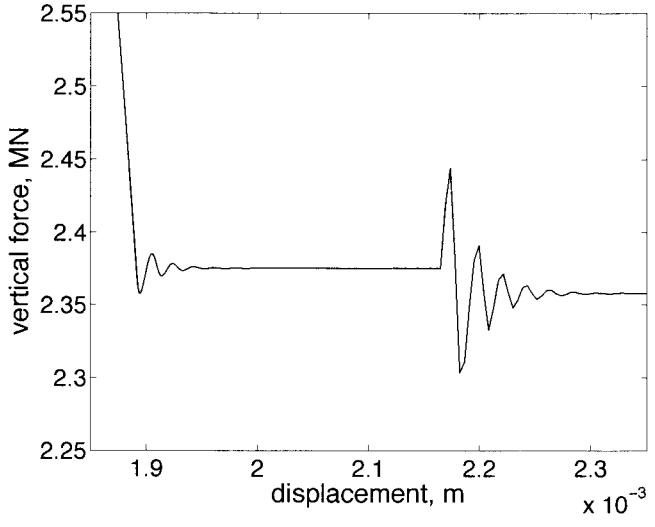

Figure 3.14: Close-up of oscillations in force-displacement curve for GeoModel. Since the material is stiffer, there is less oscillation than the gabbro example.

than 45 degrees, is less than that predicted for the gabbro example.

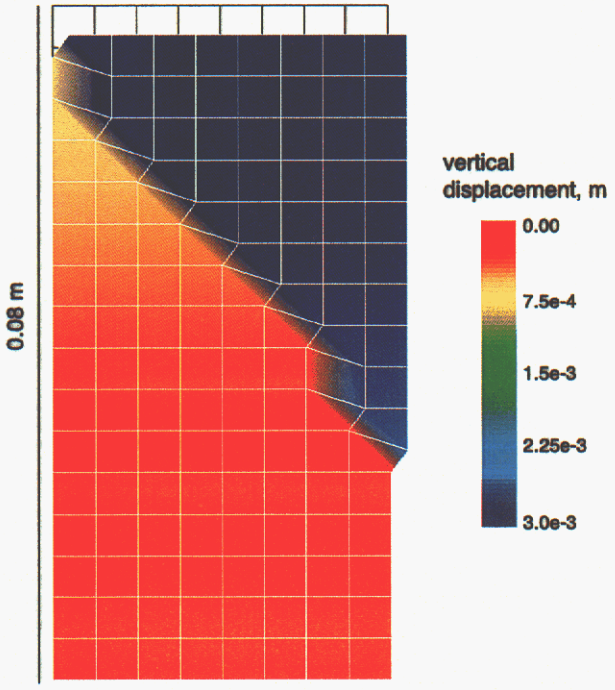

Figure 3.15: Deformed shape of plane strain compression of limestone, showing localized deformation. Note that these material properties predict a lower critical angle.

3.8 Conclusions

In this chapter we have presented a novel algorithm for implementing a general traction-displacement model into an enhanced strain element. The specific model considered combines slip weakening during nucleation of a strong discontinuity and frictional response appropriate for geomaterials and other materials exhibiting velocity- and state-dependent coefficient of friction. The constitutive model chosen to represent a variable coefficient of friction applies to slow slip velocities and laboratory-derived state and friction laws, where variations in the coefficient of friction are generally small. However, for large slips and slip rates, a much lower coefficient of friction may be activated by additional weakening mechanisms such as flash heating [81, 82]. The framework presented in this paper is a first step toward implementing such friction models, including those encountered in earthquake fault modeling. Work in this area is in progress.

Numerical examples demonstrate that the formulation converges at the rate mathematical analysis predicts. They also demonstrate some of the advantages of implementing this element into a continuum framework such as the finite element method.

Such a formulation can predict the direction and timing of crack propagation through a body as the forces redistribute. It also endows the body with a finite stiffness, which is critical for determining whether the slip along the surface is stable or unstable. A rigid approximation of the bulk material would be unable to predict these conditions.

Finally, a locking effect occurs when bands change direction as they propagate. While some of this may be physical, additional enhancements may be needed to overcome the additional resistance that the formulation artificially generates, such as that arising from an opening crack mode.

This page intentionally left blank.

Chapter 4

Conclusions and Future Work

4.1 Conclusions

This report presents a framework for the numerical modeling of shear localization in geomaterials. Using the finite element method as a basis, this framework includes the continuum elastic and elasto-plastic pre-failure behavior, a localization condition, a constitutive model for slip weakening and frictional response, and the numerical formulation and implementation of this model into a finite element with an embedded strong discontinuity. While similar frameworks have been proposed [54, 55], several specific extensions have been made.

The bifurcation condition has been used for some time for detecting the onset of localization. However, closed-form solutions for the bifurcation condition such as those described in [54] for simple models are harder to derive for more complex and accurate geomaterial models. Since the bifurcation could occur for any normal $\boldsymbol{n}$, a numerical search must be performed for a critical normal. We modify the numerical search algorithm described in [37] and [64] for nonassociative or kinematically hardening models that have nonsymmetric tangent operators.

For shear fractures, we must understand the constitutive behavior along the fracture surface after bifurcation. We have developed a combined slip-weakening and frictional model appropriate for this kind of localization. During the slip weakening phase, the cohesive strength falls as the intergranular (and sometimes intragranular) bonds are broken, and the microcracks coalesce to form a coherent macrocrack. At the same time, the frictional resistance builds, with the response becoming completely frictional after the cohesion degrades completely. The constitutive model is formulated in such a way that it can accommodate a general frictional model, and we have focused on a rate- and state-dependent friction model developed in the geosciences community.

This surface constitutive response has been embedded in the strong discontinuity element to determine the slip. The element technology allows a slip surface to be inserted at an arbitrary orientation and position within the element. The bifurcation condition gives the orientation of the surface, while the band tracking algorithm determines the location, tracing the propagation of the surface through the element. The tracking algorithm allows for multiple surfaces to propagate through the body

simultaneously.

We employ a generalized trapezoidal scheme for time integration of the constitutive equation along the slip surface to determine the slip. This scheme allows us to embed an arbitrary surface response into the element, and hence is quite general. For the constitutive model we have developed, we find that we can increase the efficiency of the algorithm by reducing the problem to a single-variable Newton-Raphson iteration. Both the general and specific formulations have the advantage that they can be implemented in a general numerical framework. The method employed only needs to specify how the shear and normal stress change with slip. A simple "stress-point" model has been implemented that assumes spatially constant traction across the surface and rigid bulk material. With some modification, the formulation is also appropriate for contact algorithms, cohesive surface formulations, extended finite elements, and meshfree methods.

Numerical examples are able to capture the slip weakening and frictional responses reported by experimental investigations and predicted by the constitutive models. The finite element implementation has the ability to capture pre-bifurcation elastic and plastic deformation, post-localization weakening, and the stable and unstable slip properties predicted by the friction model. The last result is something that could not be captured with simple rigid approximation to the bulk material, since the instability relies very much on the stiffness of the bulk material. Further examples demonstrate the ability of the formulation to handle multiple, non-intersecting bands. Under continued slip, these examples also reveal a "kinematic locking" phenomenon related to the opening of the band. Convergence in both time and space is observed, except in the case of locking phenomenon.

While this formulation has applications to several areas, one of particular interest is the formation, propagation and slip along fault systems. While there is still some work to be done, the model presented in this report lays much of the foundation and presents significant progress in many of the numerical issues associated with such a task. The ability to capture the propagation of bands and unstable slip is particularly promising.

4.2 Future work

There are several interesting ways to take this research forward. The first issue is allowing the element to overcome the locking exhibited. While one expects increased resistance on a band that is not straight, the element currently has limited means to overcome this resistance. Adding an extra opening degree of freedom to the element, and perhaps a rotational degree of freedom as well, would allow the element to slide more easily. Such modeling will also aid in more accurate modeling of faulting, where local tension, wing cracks, and other phenomena are observed. Extending

the formulation to the finite deformation regime, where the bands may rotate in space, would also help. Another extension worth investigating is the development of a three-dimensional version of the element. Such an element will allow the analysis of a broader class of problems more realistically. Research in this area is already under way [1].

One of the major motivations of this investigation is the desire to capture the initiation, propagation, and slip behavior of fault systems. While significant progress has been made, there remain some aspects of this system that are not yet adequately modeled. Temperature dependence has been shown to have a great effect on the slip behavior of faults, especially in the form of flash heating. This could be approached with a coupled thermal-mechanical model of the fault system. Fluid flow on faults also plays an important role in some cases, and the coupled fluid-slip relationship deserves exploration.

This page intentionally left blank.

References

[1] R.A. Regueiro, A.F. Fossum, R.P. Jensen, C.D. Foster, M.T. Manzari, and R.I. Borja. Computational modeling of fracture and fragmentation in geomaterials. SAND2005-5940, Sandia National Laboratories, 2005.

[2] C. D. Foster, R. A. Regueiro, A. F. Fossum, and R. I. Borja. Implicit numerical integration of a three-invariant, isotropic/kinematic hardening cap plasticity model for geomaterials. Computer Methods in Applied Mechanics and Engineering, 194(50/52):5109 – 38, 2005.

[3] A. F. Fossum and R. M. Brannon. The Sandia Geomodel: Theory and User's Guide. SAND report, Sandia National Laboratories, 2004.

[4] A. F. Fossum and J. T. Fredrich. Cap plasticity models and compactive and dilatant pre-failure deformation. In J. Girard, M. Liebman, C. Breeds, and T. Doe, editors, Pacific Rocks 2000: Rock Around The Rim, pages 1169–1176. A.A. Balkema, 2000.

[5] R. I. Borja, K. M. Sama, and P. F. Sanz. On the numerical integration of three-invariant elastoplastic constitutive models. Computer Methods in Applied Mechanics and Engineering, 192(9–10):1227–1258, 2003.

[6] C. Tamagnini, R. Castellanza, and R. Nova. A Generalized Backward Euler algorithm for the numerical integration of an isotropic hardening elastoplastic model for mechanical and chemical degradation of bonded geomaterials. International Journal for Numerical and Analytical Methods in Geomechanics, 26(10):963–1004, 2002.

[7] J. Hadamard. Lecons sur la Propagation des Ondes. Herman et fil, Paris, 1903.

[8] T. Y. Thomas. Plastic flow and fracture of solids. Academic Press, New York, 1961.

[9] A. Nadai. Plasticity. McGraw-Hill, 1931.

[10] R. Hill. General theory of uniqueness and stability in elastic-plastic solids. Journal of the Mechanics and Physics of Solids, 6(3):236 – 249, May 1958.

[11] J. W. Rudnicki and J. R. Rice. Conditions for the localization of deformation in pressure-sensitive dilatant materials. Journal of the Mechanics and Physics of Solids, 23(6):371 – 94, Dec 1975.

[12] J.R. Rice. The localization of plastic deformation. In W.T. Koiter, editor, Proceedings of The 14th Congress on Theoretical and Applied Mechanics, volume 1, pages 207–220, Delft, The Netherlands, 1976. North-Holland Publishing Company, Amsterdam.

[13] J.R. Rice. The Mechanics of Earthquake Rupture. In A.M. Dziewonski and E. Boschi, editors, Physics of the Earth's Interior, pages 555–649. North-Holland Pub. Co., Amsterdam, New York, 1980.

[14] R. I. Borja. Bifurcation of elastoplastic solids to shear band mode at finite strain. Computer Methods in Applied Mechanics and Engineering, 191(46):5287 – 314, 2002.

[15] R. I. Borja and A. Aydin. Computational modeling of deformation bands in granular media. I. geological and mathematical framework. Computer Methods in Applied Mechanics and Engineering, 193(27/29):2667 – 98, Jul 2004.

[16] R.I. Borja. Conditions for instabilities in collapsible solids including volume implosion and compaction banding. Acta Geotechnica, in press.

[17] R. I. Borja. Cam-clay plasticity. part V: a mathematical framework for three-phase deformation and strain localization analyses of partially saturated porous media. Computer Methods in Applied Mechanics and Engineering, 193(48/51):5301 – 38, Dec 2004.

[18] T. F. Wong. Shear fracture energy of westerly granite from post-failure behavior. Journal of Geophysical Research, 87(NB2):990 – 1000, 1982.

[19] J. H. Dieterich. Modeling of rock friction. I. experimental results and constitutive equations. Journal of Geophysical Research, 84(B5):2161 – 8, 1979.

[20] A. Ruina. Slip instability and state variable friction laws. Journal of Geophysical Research, 88(B12):10359 – 10370, Dec 1983.

[21] J. H. Dieterich and M. F. Linker. Fault stability under conditions of variable normal stress. Geophysical Research Letters, 19(16):1691 – 4, Aug 1992.

[22] J. R. Rice and Y. Ben-Zion. Slip complexity in earthquake fault models. Proceedings of the National Academy of Sciences of the United States of America, 93(9):3811 – 3818, 1996.

[23] F. M. Chester and N. G. Higgs. Multimechanism friction constitutive model for ultrafine quartz gouge at hypocentral conditions. Journal of Geophysical Research, 97(B2):1859 – 70, Feb 1992.

[24] M. L. Blanpied, T. E. Tullis, and J. D. Weeks. Effects of slip, slip rate, and shear heating on the friction of granite. Journal of Geophysical Research, 103(B1):489 – 511, Jan 1998.

[25] A. Needleman. Material rate dependence and mesh sensitivity in localization problems. Computer Methods in Applied Mechanics and Engineering, 67:69–85, 1988.

[26] F. H. Abed and G. Z. Voyiadjis. Plastic deformation modeling of AL-6XN stainless steel at low and high strain rates and temperatures using a combination of bcc and fcc mechanisms of metals. International Journal of Plasticity, 21(8):1618 – 39, Aug 2005.

[27] M. Jirasek and S. Rolshoven. Comparison of integral-type nonlocal plasticity models for strain-softening materials. International Journal of Engineering Science, 41(13/14):1553 – 602, Aug 2003.

[28] G. Di Luzio and Z. P. Bazant. Spectral analysis of localization in nonlocal and over-nonlocal materials with softening plasticity or damage. International Journal of Solids and Structures, 42(23):6071 – 100, Nov 2005.

[29] G. Z. Voyiadjis and R. J. Dorgan. Formulation of a gradient enhanced coupled damage-plasticity model. American Society of Mechanical Engineers, Applied Mechanics Division, AMD, 255:15 – 22, 2004 2004.

[30] G. Z. Voyiadjis and R. K. A. Al-Rub. A physically based gradient plasticity theory. International Journal of Plasticity, 22(4):654 – 84, 2006.

[31] M. T. Manzari and R. A. Regueiro. Gradient plasticity modeling of geomaterials in a meshfree environment. part I: Theory and variational formulation. Mechanics Research Communications, 32(5):536 – 46, Sep/Oct 2005.

[32] R. de Borst and L.J. Sluys. Localisation in a Cosserat continum under static and dynamic loading conditions. Computer Methods in Applied Mechanics and Engineering, 90:805–827, 1991.

[33] F. Armero. Large-scale modeling of localized dissipative mechanisms in a local continuum: applications to the numerical simulation of strain localization in rate-dependent inelastic solids. Mechanics of Cohesive-Frictional Materials, 4(2):101 – 31, Mar 1999.

[34] P. Wriggers. Computational Contact Mechanics. Wiley: Chichester, 2002.

[35] T. A. Laurson. Computational Contact and Impact Mechanics. Springer: Berlin, New York, Heidelberg, 2002.

[36] P. A. Klein, J. W. Foulk, E. P. Chen, S. A. Wimmer, and H. J. Gao. Physics-based modeling of brittle fracture: cohesive formulations and the application of meshfree methods. Theoretical and Applied Fracture Mechanics, 37(1/3):99 – 166, Dec 2001.

[37] M. Ortiz, Y. Leroy, and A. Needleman. A finite element method for localized failure analysis. Computer Methods in Applied Mechanics and Engineering, 61(2):189 – 214, Mar 1987.

[38] J. C. Simo and F. Armero. Geometrically non-linear enhanced strain mixed methods and the method of incompatible modes. International Journal for Numerical Methods in Engineering, 33(7):1413 – 1449, May 1992.

[39] J. C. Simo, J. Oliver, and F. Armero. An analysis of strong discontinuities induced by strain-softening in rate-independent inelastic solids. Computational Mechanics, 12:277 – 296, 1993.

[40] F. Armero and K. Garikipati. An analysis of strong discontinuities in multiplicative finite strain plasticity and their relation with the numerical simulation of strain localization in solids. International Journal of Solids and Structures, 33(20/22):2863 – 85, Aug 1996.

[41] F. Armero and C. Callari. Analysis of strong discontinuities in a saturated poro-plastic solid. International Journal for Numerical Methods in Engineering, 46(10):1673 – 1698, 1999.

[42] C. Callari and F. Armero. Finite element methods for the analysis of strong discontinuities in coupled poro-plastic media. Computer Methods in Applied Mechanics and Engineering, 191(39/40):4371 – 400, 2002.

[43] F. Armero and J. Park. An analysis of strain localization in a shear layer under thermally coupled dynamic conditions. part 2: Localized thermoplastic models. International Journal for Numerical Methods in Engineering, 56(14):2101 – 2133, Apr 2003.

[44] C. Callari and F. Armero. Analysis and numerical simulation of strong discontinuities in finite strain poroplasticity. Computer Methods in Applied Mechanics and Engineering, 193(27/29):2941 – 86, Jul 2004.

[45] J. Oliver. Modelling strong discontinuities in solid mechanics via strain softening constitutive equations. 1. fundamentals. International Journal for Numerical Methods in Engineering, 39(21):3575 – 600, Nov 1996.

[46] J. Oliver. Modelling strong discontinuities in solid mechanics via strain softening constitutive equations. 2. numerical simulation. International Journal for Numerical Methods in Engineering, 39(21):3601 – 23, Nov 1996.

[47] J. Oliver, A. E. Huespe, M. D. G. Pulido, and E. Chaves. From continuum mechanics to fracture mechanics: the strong discontinuity approach. Engineering Fracture Mechanics, 69(2):113 – 36, Jan 2002.

[48] J. Oliver, A. E. Huespe, and E. Samaniego. A study on finite elements for capturing strong discontinuities. International Journal for Numerical Methods in Engineering, 56(14):2135 – 61, Apr 2003.

[49] J. Oliver and A. E. Huespe. Continuum approach to material failure in strong discontinuity settings. Computer Methods in Applied Mechanics and Engineering, 193(30-32):3195 – 3220, Jul 2004.

[50] J. Oliver, A. E. Huespe, E. Samaniego, and E. W. V. Chaves. Continuum approach to the numerical simulation of material failure in concrete. International Journal for Numerical and Analytical Methods in Geomechanics, 28(7-8):609 – 632, Jun/Jul 2004.

[51] R. A. Regueiro and R. I. Borja. A finite element model of localized deformation in frictional materials taking a strong discontinuity approach. Finite Elements in Analysis and Design, 33(4):283 – 315, 1999.

[52] R. I. Borja. A finite element model for strain localization analysis of strongly discontinuous fields based on standard Galerkin approximation. Computer Methods in Applied Mechanics and Engineering, 190(11/12):1529 – 49, Dec 2000.

[53] R. I. Borja, R. A. Regueiro, and T. Y. Lai. FE modeling of strain localization in soft rock. Journal of Geotechnical and Geoenvironmental Engineering, 126(4):335 – 343, Apr 2000.

[54] R. A. Regueiro and R. I. Borja. Plane strain finite element analysis of pressure sensitive plasticity with strong discontinuity. International Journal of Solids and Structures, 38(21):3647 – 72, May 2001.

[55] R. I. Borja and R. A. Regueiro. Strain localization in frictional materials exhibiting displacement jumps. Computer Methods in Applied Mechanics and Engineering, 190(20/21):2555 – 80, 2001.

[56] R. I. Borja. Finite element simulation of strain localization with large deformation: Capturing strong discontinuity using a Petrov-Galerkin multiscale formulation. Computer Methods in Applied Mechanics and Engineering, 191(27/28):2949 – 78, 2002.

[57] M. Jirasek. Comparative study on finite elements with embedded discontinuities. Computer Methods in Applied Mechanics and Engineering, 188(1/3):307 – 30, Jul 2000.

[58] T. Jirasek and T. Zimmermann. Embedded crack model. I. basic formulation. International Journal for Numerical Methods in Engineering, 50(6):1269 – 90, Feb 2001.

[59] R. Larsson, P. Steinmann, and K. Runesson. Finite element embedded localization band for finite strain plasticity based on a regularized strong discontinuity. Mechanics of Cohesive-Frictional Materials, 4(2):171 – 94, Mar 1999.

[60] P. Steinmann. Finite element formulation for strong discontinuities in fluid-saturated porous media. Mechanics of Cohesive-Frictional Materials, 4(2):133 – 152, Mar 1999.

[61] T. Belytschko, N. Moes, S. Usui, and C. Parimi. Arbitrary discontinuities in finite elements. International Journal for Numerical Methods in Engineering, 50(4):993 – 1013, 2001.

[62] M. Stolarska, D. L. Chopp, N. Moes, and T. Belytschko. Modelling crack growth by level sets in the extended finite element method. International Journal for Numerical Methods in Engineering, 51(8):943 – 60, Jul 2001.

[63] E. Samaniego and T. Belytschko. Continuum-discontinuum modelling of shear bands. International Journal for Numerical Methods in Engineering, 62(13):1857 – 72, Apr 2005.

[64] G. N. Wells and L. J. Sluys. Analysis of slip planes in three-dimensional solids. Computer Methods in Applied Mechanics and Engineering, 190(28):3591 – 606, Mar 2001.

[65] G. N. Wells and L. J. Sluys. A new method for modelling cohesive cracks using finite elements. International Journal for Numerical Methods in Engineering, 50(12):2667 – 82, Apr 2001.

[66] J. Mosler and G. Meschke. Embedded crack vs. smeared crack models: A comparison of elementwise discontinuous crack path approaches with emphasis on mesh bias. Computer Methods in Applied Mechanics and Engineering, 193(30-32):3351 – 3375, Jul 2004.

[67] E. M. Anderson. The Dynamics of Faulting and Dyke Formation with Application to Britain. Edinburgh, Oliver and Boyd Ltd., 1951.

[68] R. H. Sibson. Earthquakes and rock deformation in crustal fault zones. Annual Review of Earth and Planetary Sciences, 14:149 – 175, 1986.

[69] B.A. Bolt. Causes of earthquakes. In R.L.Wiegel, editor, Earthquake Engineering, pages 21–45. Prentice-Hall, N.J., 1970.

[70] C. H. Scholz. The Mechanics of Earthquakes and Faulting. Cambridge University Press, Cambridge, 1990.

[71] J. W. Rudnicki. Fracture-mechanics applied to the earth's crust. Annual Review of Earth and Planetary Sciences, 8:489 – 525, 1980.

[72] R. H. Sibson. Earthquake faulting as a structural process. Journal of Structural Geology, 11(1/2):1 – 14, 1989.

[73] G. I. Barenblatt. The mathematical theory of equilibrium cracks in brittle fracture. Advances in Applied Mechanics, 7:55–129, 1963.

[74] D. S. Dugdale. Yielding of steel sheets containing slits. Journal of the Mechanics and Physics of Solids, 8(2):100 – 104, May 1960.

[75] K.H. Swindon B.A. Bilby, A.H. Cottrell. The spread of plastic yield from a notch, Proceedings of the Royal Society of London. Proceedings of the Royal Society of London, Ser A272:304–314, 1963.

[76] Y. Ida. Cohesive force across the tip of a longitudinal-shear crack and Griffith's specific surface energy. Journal of Geophysical Research, 77(20):3796 – 805, 1972.

[77] A. C. Palmer and J. R. Rice. Growth of slip surfaces in progressive failure of over-consolidated clay. Proceedings of the Royal Society of London Series A-Mathematical Physical and Engineering Sciences, 332(1591):527 – 548, 1973.

[78] F. Rummel, H. J. Alheid, and C. Frohn. Dilatancy and fracture induced velocity changes in rock and their relation to frictional sliding. Pure and Applied Geophysics, 116(4/5):743 – 64, 1978.

[79] P. G. Okubo and J. H. Dieterich. Effects of physical fault properties on frictional instabilities produced on simulated faults. Journal of Geophysical Research, 89(B7):5817 – 27, 1984.

[80] T.F. Wong. On the normal stress dependence of the shear fracture energy. In S. Das, J. Boatwright, and C.H. Scholz, editors, Earthquake Source Mechanics, Geophys. Monograph 37, Maurice Ewing Vol. 6, pages 1–11. American Geophysical Union, 1986.

[81] N. Lapusta. Modes of dynamic rupture propagation and rupture front speeds in earthquake models that account for dynamic weakening mechanisms. EOS Trans. AGU, 86(52):Abstract S34A–07, 2005.

[82] J. R. Rice. Heating and weakening of faults during earthquake slip. Journal of Geophysical Research, in press.

[83] M.S. Paterson. Rock deformation experimentation. In A. G. Duba, W. B. Durham, J. W. Handin, and H. F. Wang, editors, The Brittle-Ductile Transition in Rocks: Geophysical Monograph 56, page 243. American Geophysical Union, Washington, D.C., 1990.

[84] J. C. Jaeger and N. G. W. Cook. Fundamentals of Rock Mechanics. Chapman and Hall, London, 1969.

[85] B. Evans, J. T. Fredrich, and T. F. Wong. The brittle-ductile transition in rocks: recent experimental and theoretical progress. In A. G. Duba, W. B. Durham, J. W. Handin, and H. F. Wang, editors, The Brittle-Ductile Transition in Rocks: Geophysical Monograph 56, page 243. American Geophysical Union, Washington, D.C., 1990.

[86] J. Mandel. Conditions de stabilité et postulat de Drucker. In Proceedings IUTAM Symposium on Rheology and Soil Mechanics, pages 58–68. Springer-Verlag, Berlin, 1966.

[87] W. R. Wawersik and W.F. Brace. Post- failure behavior of a granite and diabase. Rock Mech Felsmech Mec Roches, 3(2):61 – 85, Jun 1971.

[88] W. R. Wawersik and C. Fairhurs. Study of brittle rock fracture in laboratory compression experiments. International Journal of Rock Mechanics and Mining Science, 7(5):561 – 75, Sept 1970.

[89] M. Ohnaka, M. Akatsu, H. Mochizuki, A. Odedra, F. Tagashira, and Y. Yamamoto. A constitutive law for the shear failure of rock under lithospheric conditions. Tectonophyics, 277(1-3):1 – 27, Aug 1997.

[90] M. Campillo and I. R. Ionescu. Initiation of antiplane shear instability under slip dependent friction. Journal of Geophysical Research, 102(B9):20363 – 71, Sep 1997.

[91] K. Uenishi and J. R. Rice. Universal nucleation length for slip-weakening rupture instability under nonuniform fault loading. Journal of Geophysical Research, 108(B1):ESE17 – 1, 2003.

[92] J.R. Rice and M. Cocco. Seismic fault rheology and earthquake dynamics. In M.R. Handy, editor, The Dynamics of Fault Zones, Dahlem Workshop Report 95. The MIT Press, Cambridge, MA, in press.

[93] J. H. Dieterich and B. D. Kilgore. Imaging surface contacts: Power law contact distributions and contact stresses in quartz, calcite, glass and acrylic plastic. Tectonophysics, 256(1-4):219 – 239, May 1996.

[94] J. R. Rice and A. L. Ruina. Stability of steady frictional slipping. American Society of Mechanical Engineers (Paper), 50(83-APM-16), 1983.

[95] J.K. Mitchell. Fundamentals of Soil Behavior. J. Wiley and Sons, New York, NY, 2nd edition edition, 1993.

[96] N. Lapusta, J. R. Rice, Y. Ben-Zion, and G. T. Zheng. Elastodynamic analysis for slow tectonic loading with spontaneous rupture episodes on faults with rate- and state-dependent friction. Journal of Geophysical Research, 105(B10):23765 – 89, Oct 2000.

[97] R.I. Borja and C. D. Foster. Continuum mathematical modeling of slip weakening in geological systems. Journal of Geophysical Research, in review.

[98] Y. Ben-Zion and J. R. Rice. Dynamic simulations of slip on a smooth fault in an elastic solid. Journal of Geophysical Research, 102(B8):17771 – 84, Aug 1997.

[99] M. F. Linker and J. H. Dieterich. Effects of variable normal stress on rock friction: observations and constitutive equations. Journal of Geophysical Research, 97(B4):4923 – 40, Apr 1992.

[100] T. Y. Lai. Multiscale finite element modeling of strain localization in geomaterials with strong discontinuity. PhD thesis, Stanford University, Jun 2002.

[101] M.P. Boulon, P. Garnica, and P.A. Vermeer. Soil-structure interaction: FEM computations. In A.P.S. Selvaduray and M.J. Boulon, editors, Mechanics of Geomaterial Interfaces, pages 147–171. Elsevier Science, 1995.

[102] J. C. Simo and M. S. Rifai. Class of mixed assumed strain methods and the method of incompatible modes. International Journal for Numerical Methods in Engineering, 29(8):1595 – 1638, Jun 1990.

[103] T. J. R. Hughes. The Finite Element Method. Prentice-Hall: New Jersey, 1987.

This page intentionally left blank.

Appendix A

Derivative of the post–localization yield function

For completeness, we include the derivative of the time-discretized post-localization yield function (3.45) with respect to the slip rate:

$$\begin{aligned}\frac{\partial \Phi_{n+1}}{\partial \dot{\zeta}_{n+1}} = \left[(\boldsymbol{n}\otimes\boldsymbol{l})^s + \mu_{n+1}\,(\boldsymbol{n}\otimes\boldsymbol{n})\right] : \frac{\partial \boldsymbol{\sigma}_{n+1}}{\partial \dot{\zeta}_{n+1}} \\ + \frac{\partial \mu_{n+1}}{\partial \dot{\zeta}_{n+1}}\,(\boldsymbol{n}\otimes\boldsymbol{n}) : \boldsymbol{\sigma}_{n+1} - \frac{\partial c_{n+1}}{\partial \dot{\zeta}_{n+1}}\end{aligned} \tag{A.1}$$

where

$$\frac{\partial c_{n+1}}{\partial \dot{\zeta}_{n+1}} = \begin{cases} -x-y & \texttt{if} \quad 0 \le \zeta_{n+1} \le \zeta^+ \\ 0 & \texttt{if} \quad \zeta_{n+1} > \zeta^+ \end{cases} \tag{A.2}$$

and

$$x = \left(1 - \frac{\zeta_{n+1}}{\zeta^+}\right)\left(\sigma_{n+1}\frac{\partial \mu_{n+1}}{\partial \dot{\zeta}_{n+1}} + \mu_{n+1}\frac{\partial \sigma_{n+1}}{\partial \dot{\zeta}_{n+1}}\right) \tag{A.3}$$

$$y = \frac{\left(\partial \zeta_{n+1}/\partial \dot{\zeta}_{n+1}\right)}{\zeta^+}\,(\tau_0 - \mu\sigma_{n+1}) \tag{A.4}$$

$$\frac{\partial \Delta\zeta_{n+1}}{\partial \dot{\zeta}_{n+1}} = \beta_\zeta \Delta t \tag{A.5}$$

$$\frac{\partial \boldsymbol{\sigma}_{n+1}}{\partial \dot{\zeta}_{n+1}} = -\boldsymbol{c}^e : \left(\nabla f^h \otimes \boldsymbol{m}\right)\frac{\partial \Delta\zeta_{n+1}}{\partial \dot{\zeta}_{n+1}} \tag{A.6}$$

If we define

$$\alpha = \frac{1}{2V^*} \exp\left(\frac{\mu^* + B\ln\left(\theta_{n+1}/\theta^*\right)}{A}\right) \tag{A.7}$$

then

$$\frac{\partial \mu_{n+1}}{\partial \dot{\zeta}_{n+1}} = \frac{A}{\sqrt{1+\left(\dot{\zeta}_{n+1}\alpha\right)^2}} * \left(\alpha + \dot{\zeta}_{n+1}\alpha\frac{B}{A\theta}\frac{\partial \theta_{n+1}}{\partial \dot{\zeta}_{n+1}}\right) \tag{A.8}$$

$$= \frac{A\alpha}{\sqrt{1+\left(\dot{\zeta}_{n+1}\alpha\right)^2}} * \left(1 + \frac{\dot{\zeta}_{n+1}B}{A\theta_{n+1}}\frac{\partial \theta_{n+1}}{\partial \dot{\zeta}_{n+1}}\right) \tag{A.9}$$

$$\frac{\partial \theta_{n+1}}{\partial \dot{\zeta}_{n+1}} = -\frac{\beta_\theta \Delta t D_c \left\{\theta_n + \Delta t\left[\left(1-\beta_\theta\right)\dot{\theta}_n + \beta_\theta\right]\right\}}{\left(D_c + \beta_\theta \dot{\zeta}_{n+1}\Delta t\right)^2} \tag{A.10}$$

DISTRIBUTION:

1 Prof. R.I. Borja
Department of Civil and Environmental Engineering
Terman Engineering Center M42
Stanford University
Stanford, California 94305-4020

1 Prof. R.A. Regueiro
Department of Civil, Environmental, and Architectural Engineering
1111 Engineering Dr.
428 UCB, ECOT 441
Boulder, CO 80309-0428

1 Dr. C.D. Foster
Technical University of Catalonia (UPC)
Campus Nord UPC, Edifici C1
Carrer Jordi Girona, 1-3
08034 Barcelona, Spain

1 MS 0372
J. Pott, 1524

1 MS 0372
D.C. Hammerand, 1524

1 MS 0372
J.T. Ostien, 1524

1 MS 0372
W.M. Scherzinger, 1524

1 MS 0380
H.S. Morgan, 1540

1 MS 0751
T.W. Pfeifle, 6117

1 MS 0751
R.M. Brannon, 6117

1 MS 0751
A.F. Fossum, 6117

1 MS 0824
W.L. Hermina, 1510

1 MS 0825
C.W. Peterson, 00003

1 MS 0847
J.M. Redmond, 1526

1 MS 0886
J.V. Cox, 1526

1 MS 0888
R.S. Chambers, 1526

1 MS 0888
E.D. Reedy Jr., 1526

1 MS 1070
P.L. Reu, 1526

1 MS 1070
H. Sumali, 1526

1 MS 1322
J.B. Aidun, 1435

1 MS 1411
H.E. Fang, 1814

1 MS 1411
C.C. Battaile, 1814

1 MS 1411
E.A. Holm, 1814

1 MS 1411
V. Tikare, 1814

1 MS 9001
P.J. Hommert, 8000

1 MS 9001
P.A. Spence, 8000

1 MS 9004
J.M. Hruby, 8100

1 MS 9035
W.R. Even Jr., 8220

1 MS 9042
M.L. Chiesa, 8774

1 MS 9042
J.A.W. Crowell, 8774

1 MS 9042
J.J. Dike, 8774

1 MS 9042
M.D. Jew, 8774

1 MS 9042
B.L. Kistler, 8774

1 MS 9042
Y. Ohashi, 8774

1 MS 9042
T.R. Shelton, 8774

1 MS 9042
E.P. Chen, 8776

1 MS 9042
D.J. Bammann, 8776

1 MS 9042
A.A. Brown, 8776

1 MS 9042
J.W. Foulk III, 8776

10 MS 9042
J.A. Zimmerman, 8776

1 MS 9153
C.L. Knapp, 8200

1 MS 9161
A.E. Pontau, 8750

1 MS 9161
S.W. Allendorf, 8756

1 MS 9161
J.L. Lee, 8759

1 MS 9402
J.E.M Goldsmith, 8772

1 MS 9402
X. Zhou, 8776

1 MS 9403
T.J. Shepodd, 8778

1 MS 9404
D.M. Kwon, 8770

1 MS 9405
R.W. Carling, 8700

1 MS 9405
S. Aubry, 8776

1 MS 9405
T.D. Nguyen, 8776

1 MS 9409
R.E. Jones, 8776

1 MS 9409
C.D. Moen, 8757

2 MS 9018
Central Technical Files, 8945-1

2 MS 0899
Technical Library, 4536

1 MS 0123
D. Chavez, LDRD Office, 1011